Design Principles for Trap-Free Cesium Lead Halide Perovskite Nanocrystals

By

David Porter Nenon

A dissertation submitted in partial satisfaction of the

requirements for the degree of

Doctor of Philosophy

in

Chemistry

in the

Graduate Division

of the

University of California, Berkeley

Committee in charge:

Professor A. Paul Alivisatos, Chair

Professor Phillip Geissler

Professor Feng Wang

Spring 2020

Abstract

Design Principles for Trap-Free Cesium Lead Halide Perovskite Nanocrystals

by

David Porter Nenon

Doctor of Philosophy in Chemistry

University of California, Berkeley

Professor A. Paul Alivisatos, Chair

This dissertation will introduce a general surface passivation mechanism for cesium lead halide perovskite materials ($CsPbX_3$, X = Cl, Br, I) that is supported by a combined experimental and theoretical study of the nanocrystal surface chemistry. A variety of spectroscopic methods are employed together with *ab initio* calculations to identify surface halide vacancies as the predominant source of charge trapping. The number of surface traps per nanocrystal is quantified by ^{1}H NMR spectroscopy, and that number is consistent with a simple trapping model in which surface halide vacancies create deleterious under-coordinated lead atoms. These halide vacancies exhibit trapping behavior that differs between $CsPbCl_3$, $CsPbBr_3$, and $CsPbI_3$.

Ab initio calculations suggest that introduction of anionic X-type ligands can produce trap-free band gaps by altering the energetics of lead-based defect levels. General rules for selecting effective passivating ligand pairs are introduced by considering established principles of coordination chemistry. Introducing softer, anionic, X-type Lewis bases that target under-coordinated lead atoms results in absolute quantum yields approaching unity and monoexponential luminescence decay kinetics, thereby indicating full trap passivation. This work provides a systematic framework for preparing highly luminescent $CsPbX_3$ nanocrystals with variable compositions and dimensionalities, thereby improving fundamental understanding of these materials and informing future synthetic and post-synthetic efforts towards trap-free $CsPbX_3$ nanocrystals.

Acknowledgements

This dissertation is dedicated to my family, friends, and loved ones – you bring unbridled joy to my life, and I am deeply grateful for your company during graduate school. It has been an amazing ride.

I would also like to thank my advisor, Paul Alivisatos, for leading by example. Your humility and joy for learning continue to inspire me. I would also like to thank Jacob Olshansky for his outstanding mentorship, along with the countless other members of the research community who have invested in my growth as an independent scientist.

Table of Contents

List of Figures

List of Tables

Chapter 1 : Introduction

1.1: Motivation

Over the past seventy years, semiconducting materials have profoundly altered the world around us. These materials generate renewable electricity from sunlight, serve as the physical foundation for the digital age, capture images with unprecedented spatial and temporal resolution, and form diodes that emit light with high efficiencies, to name but a few applications. The pace of progress has been blistering – silicon photovoltaics have transformed from a prohibitively expensive technology to a commodity good, and the average smartphone now has more computing power than NASA had available for the moon landing in 1969.

In the arena of scientific research, semiconductors that have been shrunk down to a few tens or hundreds of atoms in diameter have established their own revolution, giving rise to the field of nanoscience. In addition to founding a mature field of research, semiconductor nanocrystals, also known as quantum dots, have seen commercial success as downconverting fluorophores in high-definition displays. However, material quality typically lags behind that of more established bulk semiconductors such as silicon and gallium arsenide, precluding quantum dots from finding success in a broader range of key applications like photovoltaics. This dissertation will explore a relatively new class of semiconducting nanocrystals that have the potential to serve as outstanding materials for photonic and optoelectronic technologies and will enumerate methods to optimize their photophysical properties.

1.2: Photophysics of Semiconductor Nanocrystals

Nanocrystals are commonly described as building blocks, as they can be joined together to form a wide array of useful architectures. In a general sense, optimal material building blocks should be: 1) tunable, 2) uniform, and 3) high-quality. Currently, state-of-the-art quantum dots routinely fulfill the former two criteria. Properties vary significantly with size,[1-7] as illustrated in Figure 1.1, which offers excellent tunability, and a series of synthetic advances in the 1990's and early 2000's largely solved the problem of uniformity – nanocrystal reactions now routinely yield a sufficiently monodisperse limit in a wide variety of materials.[8-13] However, it should be noted that a report that was published during the writing of this dissertation found that even for nanocrystal ensembles with narrow size distributions, individual nanocrystals are remarkably heterogeneous at the atomic level,[14] indicating that there is still room for substantial improvement in both material quality and uniformity.

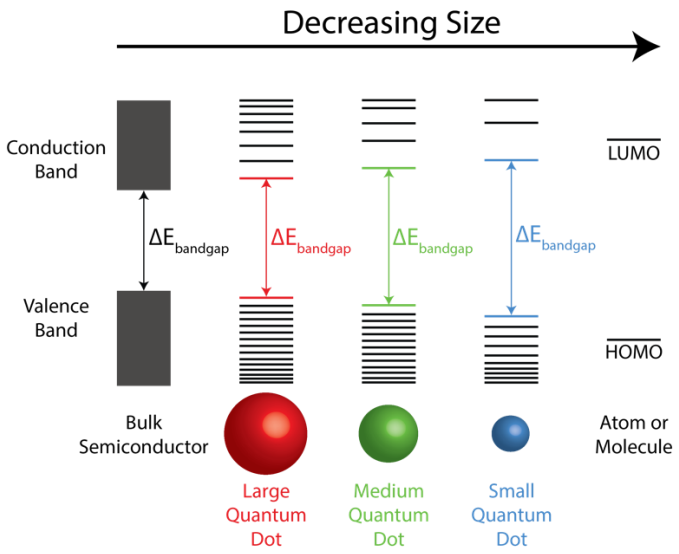

Figure 1.1: Schematic representation of the size-dependent bandgap of quantum dots. As a semiconductor is shrunk down to the nanoscale, electronic states at the band edge become discretized. The magnitude of this effect is increasingly pronounced in smaller nanocrystals, which are more akin to the entirely discrete states of atoms and molecules. Larger nanocrystals have lower bandgap energies than do smaller nanocrystals, which can emit in the blue and violet regions of the visible spectrum.

The outstanding tunability of quantum dots arises directly from their size – physical dimensions on the order of a few nanometers makes these objects larger than their atomic and molecular counterparts, but far smaller than their bulk analogs, as illustrated in Figure 1.1. The result is an electronic structure that marries the unprecedented tunability of molecules with desirable properties of the bulk, namely broadband absorption and delocalized charge carriers.

Molecular orbital theory can be used to understand how the band structure of extended solids arises naturally as atoms are bonded together in multiple dimensions,[15] and thus also to understand the hybrid molecular-bulk electronic structure of quantum dots presented in Figure 1.1. When two atoms are brought together to form a chemical bond, new molecular orbitals are formed from linear combinations of constituent atomic orbitals. Constructive and destructive interference lead to interactions that are stabilizing and destabilizing, respectively, which gives rise to an energetic gap between the newly formed orbitals. The magnitude of this splitting, or dispersion, is related to the strength of the overlap between the interacting orbitals. The relationship is direct – stronger nearest neighbor interactions yield more significant dispersion.

Extending this exercise to an infinite one-dimensional chain of atoms results in a continuum of states known as a band. However, chemical intuition suggests that this infinite linear structure is not the most stable one, and thus the system would be expected to undergo a symmetry-breaking distortion that lowers the overall energy by maximizing bonding interactions. In molecular chemistry, this is known as a Jahn-Teller distortion.[16] To solid-state physicists, it goes by the name of a Peierls distortion. The electronic consequences of this structural rearrangement are immense: although states at the top and bottom of the band are virtually unaffected, states near the middle of the band are significantly stabilized or destabilized. The result is the opening of a

forbidden energy region in the middle of the original band, which is now split into two; termed the bandgap, this feature is a defining property of semiconductors. More generally, bands arise from different molecular orbitals interacting in different ways, and do not necessarily require an alternating bond distortion.

The splitting of the original band into two bands, separated by the bandgap energy, helps to explain the size-dependent properties of quantum dots. On a fundamental level, material properties will change dramatically with size when the spacing between electronic states is significantly larger than the available thermal energy.[17] In semiconductors, the relevant energy level spacings are those between the band-edge states, which lie above and below the bandgap and the Fermi level. Analogous to the frontier orbitals that determine structure and reactivity of molecules,[18] these edge states dominate the properties of semiconductors. As a material grows, the center of the band forms first and the edges form last, thus it is the edge states that will vary significantly with size. As such, semiconductor clusters can exhibit size-dependent properties even in structures with several thousand atoms. In contrast, the Fermi level of metals cuts through the center of the band, which resembles a continuum even in clusters with only a few metal atoms. Thus, meaningful size dependence in metals is limited to molecular sizes and cryogenic temperatures.

The understanding of size-dependent optical properties of semiconductor nanocrystals was further advanced by Louis Brus in 1985, with the application of "particle in a box" from elementary quantum mechanics to quantitatively describe how electronic wavefunctions and corresponding physical observables such as bandgap depend directly on nanocrystal size.[19] A deeper understanding of how the density of states changes with size also provided a foundation for interpreting various aspects of quantum confinement – for example, quantum dots display narrow fluorescence linewidths because the wavefunctions that would be associated with a series of similar optical transitions in the bulk are now compressed into a single, intense transition.[20] These sharp linewidths manifest themselves as highly pure colors, which has led to the adoption of nanocrystals for high-definition displays.

In a simple picture, the first successful fabrication of nanoscale semiconductors might have yielded an ensemble of extremely luminescent particles. Following the absorption of a photon, photoexcited carriers are now confined to an extremely small volume with binding energies that are significantly higher than those of room temperature thermal fluctuations – together, these conditions strongly favor the outcome where charges recombine by emitting a photon. This stands in stark contrast to a bulk semiconductor, where photoexcitation yields charges that readily dissociate at room temperature and then separate into the effectively infinite volume of the crystal. As will be described in detail in the following paragraphs, the competition between photon-producing recombination events and those that produce heat instead determines the efficiency of luminescence, which is dubbed the photoluminescence quantum yield (PLQY). The PLQY values of prototypical nanocrystals were quite poor, and indeed, many materials still struggle in this area. Solutions to this problem, such as those proposed in this dissertation, depend critically on a detailed understanding of excited state dynamics in quantum dots.

Semiconductors can be excited by the absorption of photons with energies greater than or equal to the bandgap, as shown in Figure 1.2. An electron is promoted from the ground state

(valence band) to the excited state (conduction band), leaving a positively charged hole in its place. This Coulombically bound electron-hole pair, known as an exciton, rapidly (typically picoseconds) thermalizes to the band edge by releasing phonons into the crystal. At some later time (nanoseconds), the charges recombine, and the system is returned to the ground state. The nature of charge recombination is critical, as charges can either recombine radiatively by emitting a photon, or nonradiatively by emitting phonons.

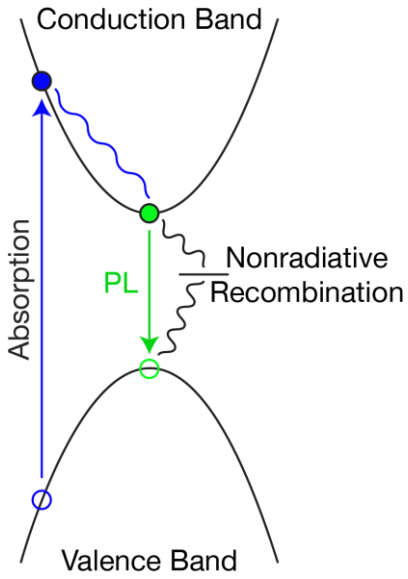

Figure 1.2: Representation of excitation and deexcitation pathways in a semiconductor material.

The competition between these two deexcitation pathways, radiative and nonradiative, gives rise to an expression for PLQY, as shown in Equation 1.1, where k_r is the radiative recombination rate and k_{nr} is the nonradiative recombination rate.

$$PLQY = \frac{k_r}{k_r + k_{nr}} \tag{1.1}$$

It should be noted that the radiative rate is an intrinsic property that arises from the electron-hole wavefunction overlap in the material as well as the transition dipole matrix elements inside each unit cell, and thus is a fixed value for a given system. As such, progress towards ultrahigh PLQY materials is synonymous with the suppression of nonradiative channels. In nanocrystals, nonradiative channels typically originate from defects and/or dangling bonds at the surface, making it essential to develop a high level of control over the surface chemistry of interest.

1.3: Quantum Dot Surface Chemistry and Band Structure

Termination of an extended inorganic solid crystal inherently creates under-coordinated atoms, making surface traps a ubiquitous challenge for nanocrystals.[21-31] The pursuit of trap-free nanocrystals is thus intimately intertwined with identification and passivation of surface defects. These defects, or structural imperfections in the crystalline lattice, have a lower coordination number than atoms in pristine bulk sections of the material, and thus are termed

"undercoordinated." An incomplete coordination sphere introduces new energy levels into the bandgap, which can trap photoexcited charges and promote nonradiative recombination, i.e. vibrational relaxation back to the ground state, which harms PLQY. Passivation is the chemical process of forming new bonds to undercoordinated atoms, which changes their energy levels to where they no longer reside in the bandgap and thus are not accessible to photogenerated electrons and holes, which improves PLQY.

A major breakthrough for high PLQY nanocrystals came in the form of a quantum dot heterostructure.[32] Specifically, enclosing a "core" material of cadmium selenide within an epitaxial "shell" of a larger bandgap material, e.g. cadmium sulfide, confines charges to the core, away from the surface where deleterious defects and dangling bonds abound. This concept is illustrated schematically in Figure 1.3.

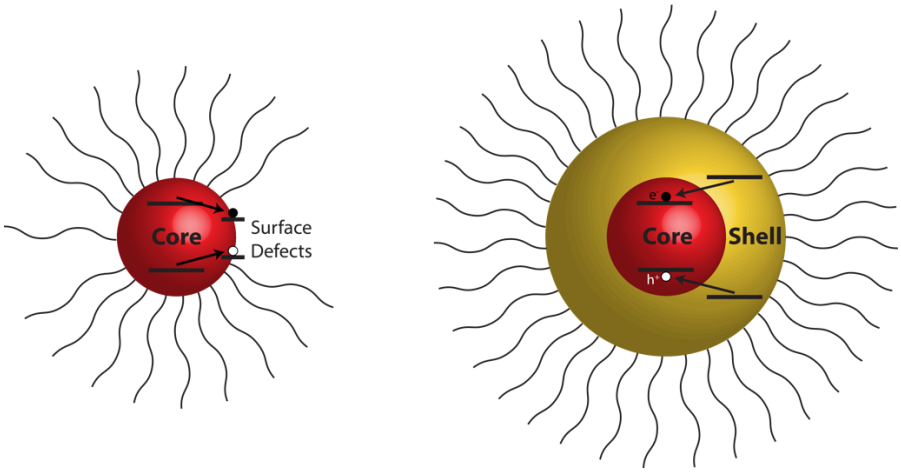

Figure 1.3: Schematic representation of core (left) and core/shell (right) nanocrystals. Solid black lines denote energy levels and wavy black lines represent typical long chain capping ligands. When a core/shell nanocrystal is excited in the shell, photoexcited electrons and holes follow the energetically favorable pathway into the core, effectively shielding them from nonradiative recombination centers at the surface.

Although the core/shell architecture was a critical breakthrough for applications that utilize quantum dots as fluorophores, the shell introduces a permanent tunneling barrier that hinders charge extraction.[33] This inability to easily inject and extract charges typically precludes these high-quality core/shell nanocrystals from serving as electronic materials in applications such as photovoltaics, where efficient charge transport is critical. Although long organic capping ligands also significantly impede charge transfer in quantum dot films, these ligands can be exchanged for much shorter ligands or removed entirely to yield a strongly coupled film.[34, 35] On the other hand, semiconductor shells cannot be readily removed after growth.

With the stated goal of high PLQY that is achieved for core/shell nanocrystals, but without the semiconductor shell, nonradiative recombination at the surface must be mitigated by the use of capping ligands.[36-39] Ligands can bind to nanocrystal surfaces in a variety of motifs, well described by the Covalent Bond Classification.[40] Figure 1.4 depicts L-, X-, and Z-type ligands,

which are classified by the number of electrons (2, 1, and 0, respectively) that the neutral ligand donates to the metal when forming a bond to the surface.

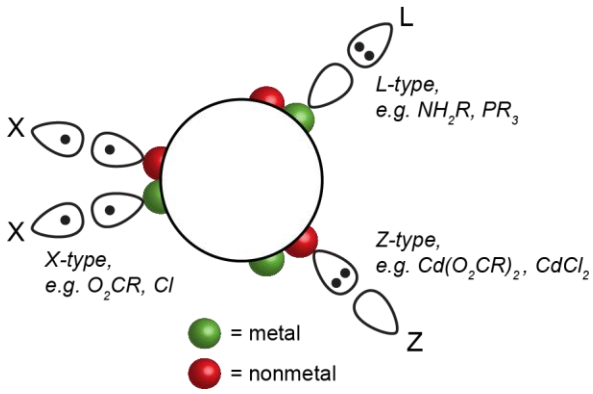

Figure 1.4: Schematic representation of the Covalent Bond Classification that was developed to describe different types of metal-ligand bonds in coordination compounds.

Although surface ligands have been shown to impart exceptional chemical functionality for prototypical nanocrystals such as cadmium selenide,[41-46] efforts to achieve high PLQY without a heterostructure geometry have been largely unsuccessful. This can be understood through the band structure of more established semiconductors, which are formed from elements whose frontier atomic orbitals are similar in energy, as depicted in Figure 1.5. It is well understood that bonding interactions between orbitals that are close in energy are more covalent in nature, yielding physically robust materials with high cohesive energies. However, such a band structure presents a major challenge to high PLQY: dangling bonds and defects, which are largely atomic in nature, present themselves deep within the bandgap. Deep trap states are remarkably effective at promoting nonradiative recombination, to the point where even a single undercoordinated atom per nanocrystal can yield PLQY < 10%. The synthetic requirements to achieve this degree of structural perfection in both the crystal and the ligand shell are extremely demanding, and the inevitable presence of equilibrium defects could preclude these core-only materials from ever achieving PLQY values that are required for more advanced photonic applications such as optical refrigeration and luminescent solar concentrators.[47-51]

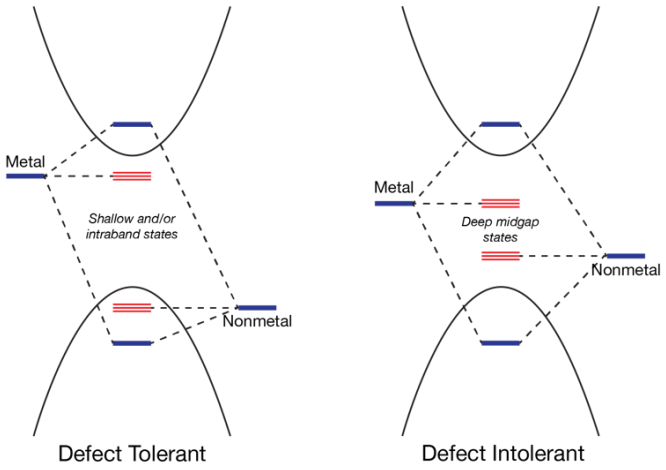

Figure 1.5: Representative band structures for defect intolerant and defect tolerant materials.

One possible solution to this problem is to consider materials beyond prototypical II-VI and III-V semiconductors, and instead seek more unusual band structures where the consequences of structural imperfections are less deleterious for PLQY: in other words, the material is tolerant to defects. This requires the constituent atomic orbitals to be close to band edge energies, or ideally, contained within the bands that form in the extended solid. Illustrated in Figure 1.5, it becomes clear that the bonding interactions in this material must be more ionic than covalent – a larger offset between atomic orbital energies, i.e. increased ionicity, can position defect levels away from the middle of the bandgap. However, it should be noted that such a structure would be expected to have a lower cohesive energy than a more covalent material, as larger energetic offsets between frontier orbitals decrease the strength of bonding interactions. Indeed, we identify this as a key scientific question: are defect tolerance and material stability fundamentally at odds?

Just a few months before the beginning of this doctoral work, nanocrystals of cesium lead halide perovskite were synthesized for the first time.[52] These materials exhibited relatively high PLQY values (60-80%) without the need for a passivating shell, which led us and others to hypothesize that $CsPbX_3$ nanocrystals could possess a desirable defect tolerant band structure.[53] This dissertation is dedicated to understanding the origin of undesirable nonradiative recombination in $CsPbX_3$ nanocrystals, and using that knowledge to enumerate and eliminate targeted defects, resulting in a systematic route to highly luminescent shell-free $CsPbX_3$ materials with variable compositions and morphologies. The proposed passivation mechanism is able to unify existing literature reports, thereby informing synthetic and post-synthetic design principles for trap-free $CsPbX_3$ nanocrystals.

Chapter 2 will describe the synthesis and characterization of cesium lead halide ($CsPbX_3$) perovskite nanocrystals, which are a relatively new material with a defect tolerant band structure.

Chapter 3 will detail an extensive experimental and theoretical investigation into the nanocrystal surface chemistry, including the development of novel ligand exchange chemistry that was used to achieve near-unity PLQY without a passivating shell.

Chapter 4 will delineate the major contributions of this work and identify promising future directions in this area of research.

Chapter 2 : Nanocrystal Synthesis and Characterization

Nanocrystals were synthesized by the well-established "hot injection" method, where organometallic precursors are rapidly injected into high-temperature solutions of surfactant ligands. The high degree of ionicity in lead halide perovskite materials leads to reaction kinetics that are significantly faster than in the syntheses of prototypical II-VI materials.[52]

2.1: Synthetic Protocols

Chemicals. Cesium carbonate (99.9%), 1-octadecene (90%), oleic acid (90%), oleylamine (70%), lead(II) bromide (99.999%), lead(II) chloride (99.999%), lead(II) iodide (99.999%), lead(II) oxide (99.999%), anhydrous toluene (99.8%), anhydrous ethyl acetate (99.8%), anhydrous hexanes (>99%), anhydrous tetrahydrofuran (>99%), didodecyldimethylammonium bromide (98%), mesitylene (>99.8%), benzoic acid (>99.5%), benzylamine (>99%), decylamine (95%), myristic acid (>99%), hexylphosphonic acid (95%), 2-ethyl-1-hexylamine (98%), fluoroacetic acid (95%), difluoroacetic acid (98%), trifluoroacetic acid (99%), methanesulfonic acid (>99%), tri-*n*-octylphosphine (97%), butyric acid (>99%), lead(II) nitrate (>99%), lead(II) hydroxide (99%), cesium acetate (>99.99%), toluene-d_8 (>99%), nickel(II) chloride hexahydrate (>97%), and zinc dust (>98%) were purchased from Sigma-Aldrich and used as received. Ethyliododifluoroacetate (96%) was purchased from Matrix Scientific and used as received. 2,2-difluorononanoic acid was synthesized from ethyliododifluoroacetate and 1-octadecene following a previously reported procedure.[54, 55]

Nanocrystal Synthesis and Isolation. $CsPbBr_3$ nanocrystals were synthesized following a previously reported procedure,[52] with slight modifications. Typically, anhydrous ODE (5 mL) and $PbBr_2$ (0.188 mmol) were loaded into a 3-neck flask inside of a glovebox, and the flask was then transferred to a Schlenk line and dried/degassed under vacuum at 110 °C for 15-20 minutes. Dried oleic acid (0.5 mL) and oleylamine (0.6 mL) were then injected under dry argon gas and the temperature was raised to 140 °C to complex the $PbBr_2$ salt. Following complete dissolution of $PbBr_2$, which we found to occur within 15-20 minutes, the temperature was raised to 155 °C in preparation for the injection of warm (~100 °C) cesium oleate solution (0.5 mL, 0.125 M). Following injection, the mixture was stirred for 5 s and then cooled using an ice-water bath. Following the synthesis, 5-10 mL of anhydrous hexanes was added to the crude solution, which was then centrifuged at 4000 rpm for 3 min to remove excessively large nanocrystals and other unwanted byproducts. The supernatant was observed to be transparent and intensely green in color. The solubility of the nanocrystals depended on the relative proportions of ODE, a poor solvent for these nanocrystals, and hexanes, a better solvent. Hexanes was removed in a step-wise fashion by flushing the surface of the solution with a stream of argon or nitrogen, and different sizes of nanocrystals were isolated from the reaction mixture. Isolated nanocrystals were resuspended in anhydrous hexanes or toluene and stored in a glovebox.

As discussed in Chapter 1, the overarching goal of this doctoral work was to develop a set of design principles for trap-free $CsPbX_3$ perovskite nanocrystals. Such principles can also be considered as a set of structure-property relationships that describe how certain structures, both physical and electronic, can either promote or mitigate energetic losses due to defect-mediated nonradiative recombination. Determination of these structure-property relationships is predicated

upon extensive characterization of both structure and optical properties, as described below. Structural techniques such as x-ray diffraction (XRD), transmission electron microscopy (TEM), x-ray photoelectron spectroscopy (XPS), and nuclear magnetic resonance spectroscopy (NMR) are complemented by optical characterization methods such as absorbance, fluorescence, and time-resolved photoluminescence lifetime spectroscopy, as well as the determination of absolute photoluminescence quantum yield (PLQY) with a home-built integrating sphere spectrofluorometer.

2.2: Structural Characterization

Following synthesis and isolation, nanocrystals were structurally characterized with a full suite of techniques that can examine the inorganic crystal as well as the surrounding organic ligand shell. Optical properties of nanocrystals are typically dominated by the organic-inorganic interface that exists at the surface, making it essential to study both components of the interface.

Transmission Electron Microscopy (TEM). TEM images were obtained with a FEI Tecnai T20 equipped with a Gatan SC200 CCD camera and LaB_6 filament operated at 200 kV.

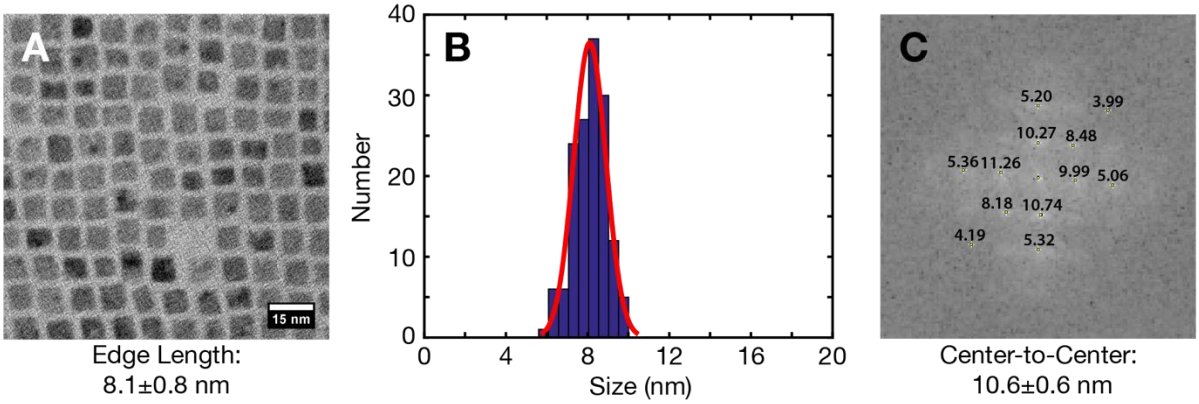

Figure 2.1: Representative A) TEM image, B) size distribution histogram, and C) fast Fourier transform of as-synthesized $CsPbBr_3$ nanocrystals.

Colloidal $CsPbBr_3$ nanocrystals exhibit cube-like morphology with typical size distributions ±10% in edge length as measured (N=75 particles) by TEM, as shown in Figure 2.1A-B. Analysis of the fast Fourier transform (FFT) shown in Figure 2.1C determines a center-to-center distance, also known as interparticle spacing, of 10.6±0.6 nm, thus indicating that organic ligands contribute 2.5±0.7 nm of spacing between these cubes of average size 8.1±0.8 nm as they arrange themselves into cubic superlattices.

Powder X-ray diffraction (XRD). Diffraction patterns of drop-cast nanocrystal samples were obtained using a Bruker D-8 GADDS diffractometer equipped with a Co Kα source and a Bruker Vantec 500 detector. Patterns were typically collected by merging frames centered at 2θ = 30, 50, and 70 degrees where each frame was collected for 40 minutes.

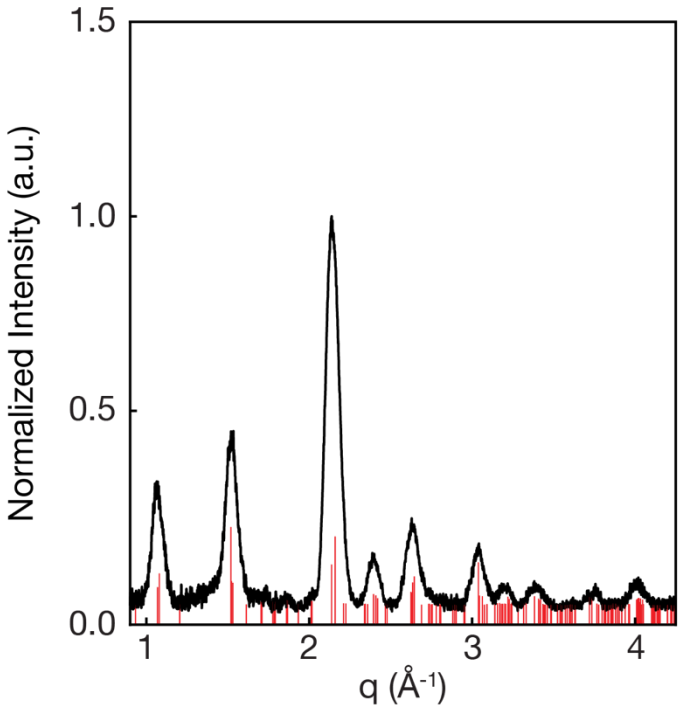

Figure 2.2: Representative X-ray diffraction pattern of $CsPbBr_3$ nanocrystals.

Figure 2.2 shows a representative diffraction pattern of $CsPbBr_3$ nanocrystals together with the simulated reference for orthorhombic $CsPbBr_3$. Although the literature initially misidentified the crystalline phase as cubic, it is now well-known that these materials crystallize in the orthorhombic phase,[56] consistent with the data presented here.

X-ray Photoelectron Spectroscopy (XPS). XPS spectra of $CsPbBr_3$ nanocrystals drop-cast on a silicon wafer were collected using Thermo Scientific K-Alpha Plus X-ray photoelectron spectrometer. The spectra were acquired with monochromatized Al Kα radiation and 400 µm beam size. Cs, Pb, and Br were quantified by fitting GL(30) peak shapes and calibrating the C 1s edge to 284.8 eV. The nanocrystals measured by XPS were slightly larger than those measured by TEM, with an average edge length of 9.4±0.5 nm.

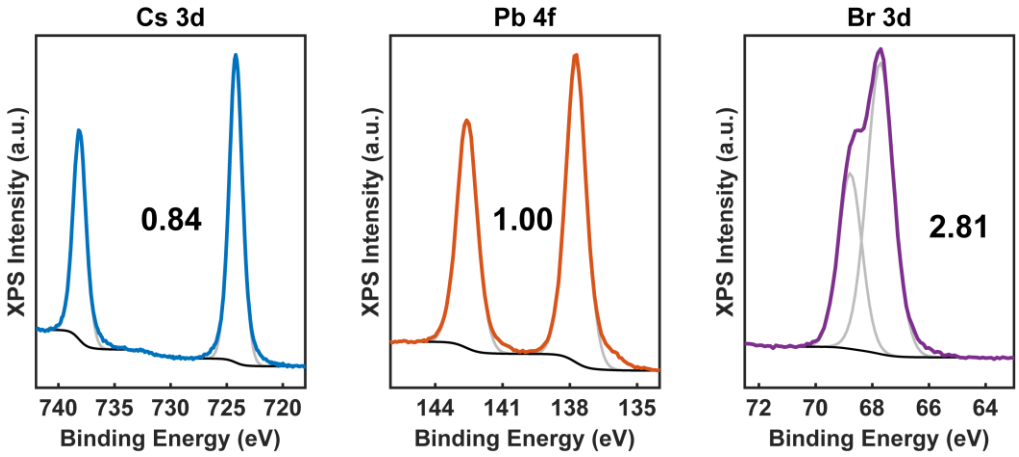

Figure 2.3: X-ray photoelectron spectroscopy results for Sample D, one of the four $CsPbBr_3$ samples measured, along with fits that yield quantitative integrations for the elemental ratio. Table 1 below contains the results for each of the four samples along with average and standard deviation statistics.

Table 1: XPS results for four $CsPbBr_3$ samples

Sample Name	Cs 3d	Pb 4f	Br 3d
Sample A	0.76	1.00	2.82
Sample B	0.76	1.00	2.86
Sample C	0.77	1.00	2.82
Sample D	0.84	1.00	2.81
Average	**0.78±0.04**	**1.00**	**2.83±0.02**

The signal measured by XPS is an exponentially surface-weighted signal. The expected stoichiometry for a pristine nanocrystal can be predicted from the edge length of the nanocube *l*, the lattice parameter *a*, and the inelastic mean free path λ. All lengths should be in nanometers. The inelastic mean free path is determined by the X-ray source energy (1486.6 eV in this case) and the binding energies of the elements, as this determines the kinetic energy of the photoelectrons. Kinetic energy can then be converted into inelastic mean free path, λ, with the universal curve:

$$E_{kinetic} = E_{source} - E_{binding} \tag{2.1}$$

$$\lambda = \frac{143}{E_{kinetic}{}^2} + 0.054 \cdot \sqrt{E_{kinetic}} \tag{2.2}$$

The inelastic mean free paths for Pb ($E_{binding}$ =140 eV) and Br ($E_{binding}$ =68 eV) are 1.98 and 2.03 nm, respectively, yielding an average inelastic mean free path for Br/Pb analysis of 2.0 nm. This value describes the attenuation of the photoelectron beam with increasing distance from the surface and will be used to determine the exponential weighting factor for each layer sampled. First, the atomic composition of each layer, and then the entire nanocrystal, must be determined. Layers are either CsX or PbX_2, and each will contribute a certain number of atoms based on the number of unit cells present in the nanocrystal. It is useful to consider the edge length of the nanocrystal in terms of unit cells, N.

$$N = \frac{l}{a} = \frac{9.4\ nm}{0.587\ nm} = 16 \tag{2.3}$$

As seen above, these samples are 16 unit cells across on average. The number of Cs, Pb, and X atoms in each layer type (for CsX termination) can now be expressed in terms of N.

CsX layer (CsX termination):

- Cs = $(N+1)^2$
- Pb = 0
- X = N^2

PbX_2 layer (CsX termination):

- Cs = 0
- Pb = N^2
- X = 2N(N+1)

This allows one to determine the exact atomic composition of these finite crystals. Each layer can then be weighted according to its distance from the surface *d*, together with the inelastic mean free path λ, as shown in Equation 2.4. The nanocrystal is terminated by CsX facets.[57]

$$I(d) = I_0 e^{\frac{-d}{\lambda}} \tag{2.4}$$

Consideration of the weighted atomic counts indicates that a pristine 9.4 nm $CsPbX_3$ nanocrystal is expected to display a Cs:Pb:X stoichiometry of 1.3:1:3.3 when measured by XPS. Thus, the experimentally measured XPS stoichiometry of 0.8:1:2.8 indicates that both Cs and X vacancies are present on the surface. As will be seen in Chapter 3, the presence of these vacancies plays a critical role in the photophysics of cesium lead halide perovskite materials.

Nuclear Magnetic Resonance (NMR) spectroscopy. NMR spectra of micromolar concentrations of $CsPbBr_3$ nanocrystals in toluene-d_8 were measured on a Bruker 700 MHz spectrometer with an inverse cryoprobe for greatly enhanced ^1H sensitivity. Quantitative measurements were collected after tuning the probe and determining the exact 90° radio frequency pulse. After a spectrum was collected, concentration was determined by integrating the peak(s) of interest against an internal standard (mesitylene) of known concentration. 2D NOESY experiments were performed using a gradient-enhanced NOESY pulse sequence, with a mixing time of 500 ms and a delay time of 7 s. Spectra were typically collected overnight (10-12 hour acquisition times) to ensure high-quality data. These results will be discussed in detail in Chapter 3.

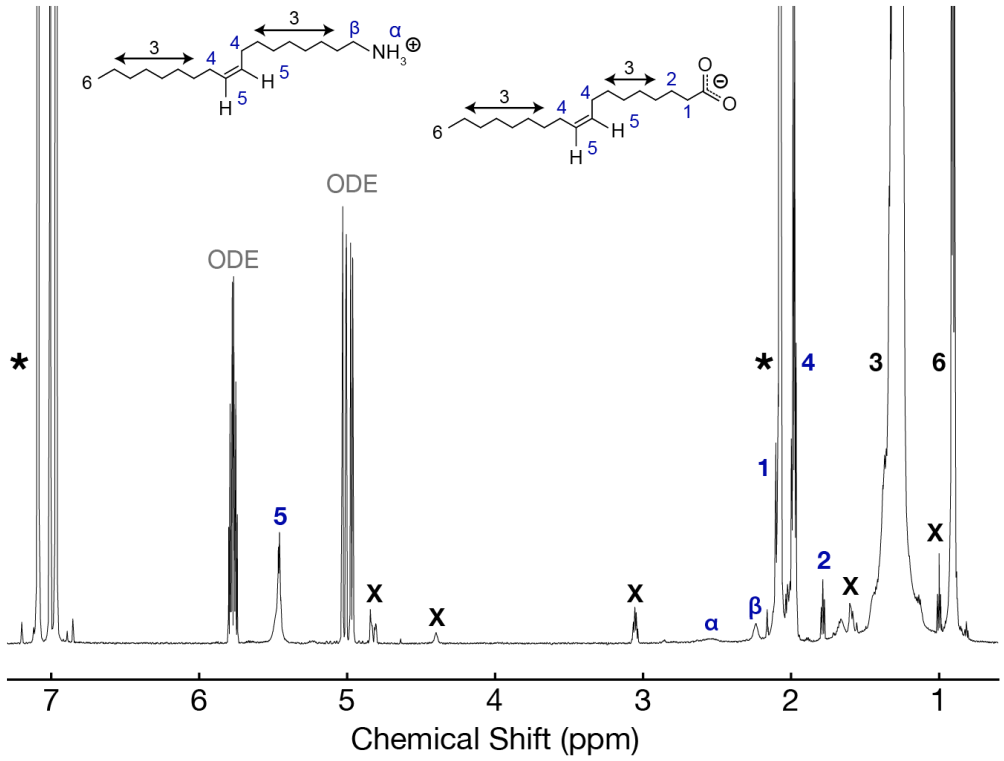

Figure 2.4: ^{1}H NMR spectrum of as-synthesized $CsPbBr_3$ nanocrystals isolated according to standard literature methods. Residual solvent (ODE) and several unknown impurities (X) are present, along with a complex mixture of oleylammonium bromide, lead oleate, oleylamine, and oleic acid (resonance 5). This highlights the need for a purification method, which will be introduced in Chapter 3. Three of the five impurities can be identified as originating from impure precursors (ODE, oleylamine, and oleic acid). The remaining impurities do not originate from a precursor, and thus are ascribed as post-synthetic impurities. The resonance around 3.06 ppm was also observed by De Roo et. al.,[58] and is presumably the amide of oleic acid and oleylamine.

Table 2: Assignment of impurities present in as-synthesized, isolated $CsPbBr_3$ nanocrystals.

Impurity Chemical Shift (ppm)	Assignment
4.83	Impurity present in ODE
4.40	Unknown (post-synthetic)
3.06	Amide (post-synthetic)
1.60	Impurity present in oleylamine
1.01	Impurity present in ODE

2.3: Optical Characterization

Optical Spectroscopy. All optical measurements were performed on dilute samples of nanocrystals in hexanes or toluene. For typical $CsPbBr_3$ nanocrystals, concentrations on the order of 1-10 nM were found to have suitable optical densities. Absorption spectra were collected on a Shimadzu UV-3600 spectrophotometer with 0.5 nm increments using the slowest scan speed.

Photoluminescence emission spectra were collected on a Horiba Jobin Yvon TRIAX 320 Fluorolog. Time-resolved fluorescence lifetimes were collected on a Picoquant Fluotime 300 with PMA 175 detector and an LDH-P-C-405 diode laser (excitation wavelength of 407.7 nm). Absolute quantum yields were determined optically using a custom integrating sphere spectrofluorometer which is described elsewhere.[51]

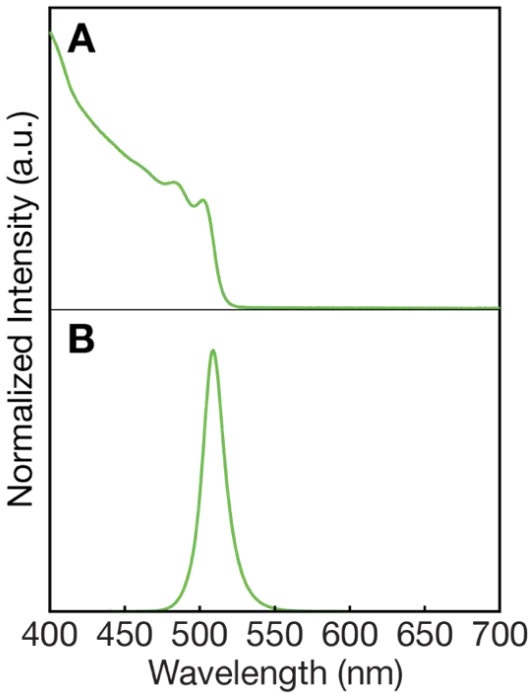

Figure 2.5: Representative A) absorbance and B) fluorescence spectra for $CsPbBr_3$ nanocrystals with emission centered around 510 nm.

The spectra shown in Figure 2.5 are typical of quantum confined semiconductors, which have minimal Stokes shifts. The narrow linewidth (~25 nm) of the fluorescence spectrum is consistent with the relatively narrow size distribution measured by TEM. Comparison against bulk $CsPbBr_3$, which has emission centered around 525 nm, indicates that these materials are in the weak confinement regime.

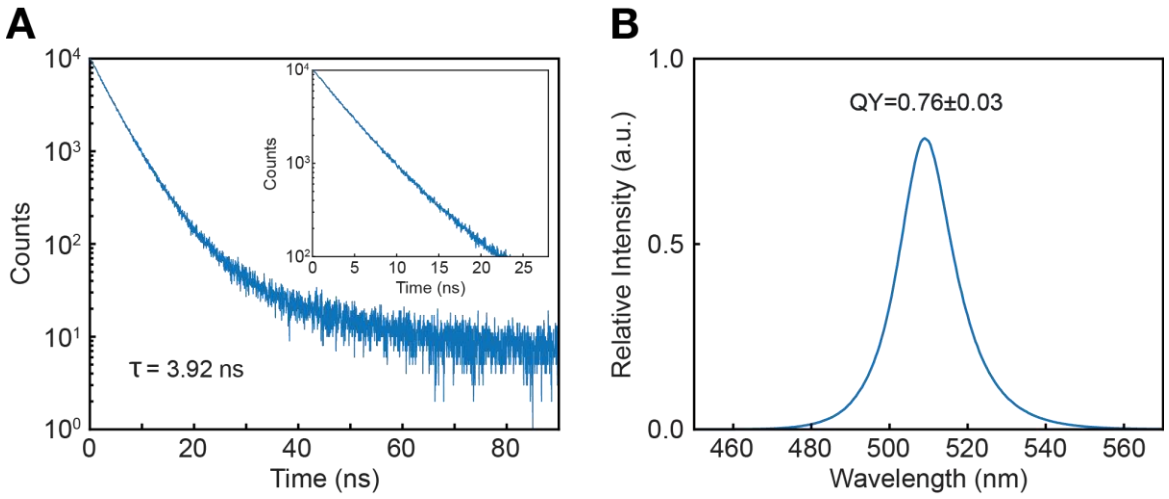

Figure 2.6: Representative A) photoluminescence decay and B) absolute photoluminescence quantum yield (PLQY) spectra for $CsPbBr_3$ nanocrystals.

Although the first two decades of the decay curve shown in the inset of Figure 2.6A are nearly monoexponential, significant deviations from this behavior are observed at later times, which is indicative of undesirable charge trapping. A measured PLQY value of 0.76±0.03 further supports that undesirable charge trapping and nonradiative recombination processes are present. A central goal of this research was to suppress and ideally eliminate these pathways, as will be described in the following chapter.

Chapter 3: Surface Chemistry, Nonradiative Recombination, and Defects

As stated in Chapter 1, the photophysical properties of semiconductor nanocrystals are typically dominated by surface effects. As such, a rational route to nanocrystals that approach PLQY values of unity depends critically on a detailed understanding of the surface chemistry. This chapter describes an intensive investigation into cesium lead halide perovskites surfaces, as well as the development of the first versatile ligand exchange method for these materials. These insights form the foundation of design principles for trap-free $CsPbX_3$ nanocrystals, which are described at the end of this chapter.

3.1: The Atomistic Nature of the $CsPbX_3$ Inorganic Surface

Following synthesis and isolation, PLQY values range from 60–90%, determined optically using an integrating sphere.[51] Although these nanocrystals are relatively bright, sub-unity PLQY values demonstrate the presence of energetic losses due to deleterious charge trapping and nonradiative recombination, thereby motivating an investigation into the origins of these processes. The underlying trapping pathways that prevent near-unity PLQY in $CsPbX_3$ nanocrystals remain a subject of debate, which hinders rational improvements of optoelectronic performance.

For metal chalcogenide nanocrystals, dangling bonds at the surface introduce localized mid-gap states that can trap charges.[21-23, 59, 60] However, *ab initio* calculations of pristine (100) $CsPbX_3$ surfaces terminated by CsX facets[57, 61-63] yield trap-free, fully delocalized electronic structures without the need for passivating ligands.[61, 64]

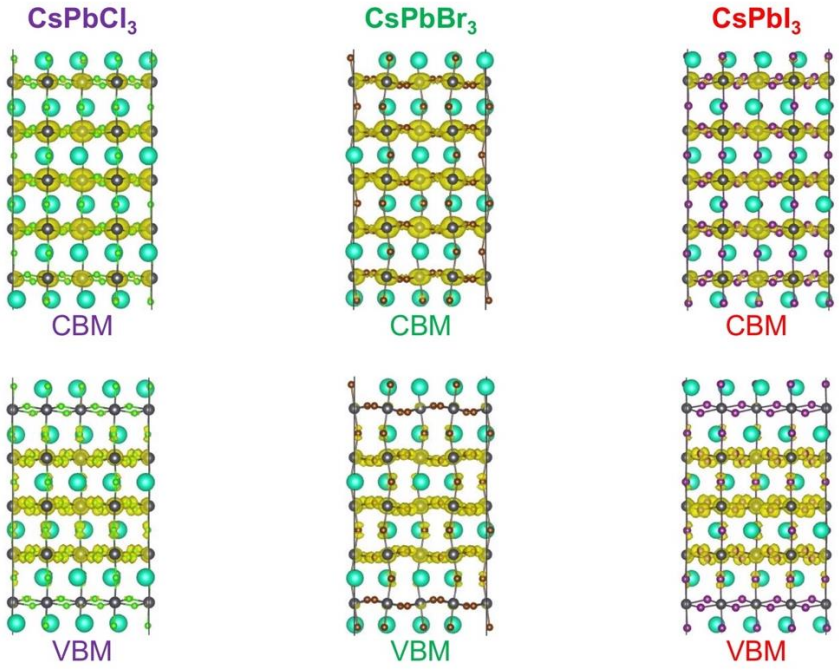

Figure 3.1: *Ab initio* calculations of $CsPbX_3$ crystal lattices terminated by pristine CsX facets. The valence band maximum (VBM) and conduction band minimum (CBM) states are fully delocalized

and the bandgap is free of midgap states, which is unusual for a crystalline lattice without any passivating ligands and could help to enable extremely high PLQY in these materials.

The computational results shown in Figure 3.1 suggest that surface dangling bond states of low-index CsX terminated $CsPbX_3$ nanocrystals lie outside of the band gap and thus do not affect photoluminescence efficiency. The observation that halide dangling bonds lie outside of the bandgap has important implications for the design of future ligand systems. From a PLQY perspective, there is no need to passivate surface atoms that do not introduce midgap states, i.e. there is no need to passivate surface halides in these nanocrystals. Thus, the binding of oleylammonium to surface halides does not improve PLQY. In contrast, it actually tends to harm PLQY by removing surface halides, which introduces trap states. Surface halides can be removed either by the facile desorption of oleylammonium halide ligand pairs, or by the formation of volatile HX mineral acids following a proton transfer from oleylammonium. For these reasons, we believe the design of future ligand systems should avoid cationic species such as oleylammonium, as they tend to remove surface halides and thus decrease PLQY.

In light of these calculations, we hypothesized that as-synthesized surfaces are not pristine, but rather contain local point defects that are a likely cause of sub-unity PLQY in $CsPbX_3$ nanocrystals. Unfortunately, the atomistic nature of the $CsPbX_3$ nanocrystal surface remains poorly understood. As such, quantitative X-ray photoelectron spectroscopy (XPS) – a surface-sensitive technique – was used to elucidate the surface stoichiometry of four different $CsPbBr_3$ samples. Based on the inelastic mean free path, the first 2.0 nm of material was probed in this experiment. For these samples, each with PLQY of 60-65%, an average surface stoichiometry of Cs:Pb:Br of $0.78\pm0.04:1:2.83\pm0.02$ was determined, as described in the previous chapter. Deviations from the expected stoichiometry support the hypothesis regarding the presence of surface point defects, namely vacancies in these systems.[53, 65, 66] However, the number of vacancies determined by XPS represents an upper bound, as the low cohesive energy of lead halide perovskite materials can lead to the loss of surface atoms when samples are transferred from the solvent phase to the vacuum, and exposed to high-energy X-rays in the ultra-high vacuum environment.[67, 68] In contrast, ambient techniques such as ^{1}H NMR spectroscopy can offer quantitative insight into surface structure without inducing sample evolution and/or degradation, as will be demonstrated later in this chapter.

Sub-stoichiometry of surface cesium is well-documented in the literature, and has been explained by a substitution mechanism where oleylammonium ions substitute into cesium vacancies.[62, 69, 70] A Pb:Br ratio that deviates from the expected stoichiometry is also well-documented in the literature, with the common interpretation being a lead-rich surface.[71, 72] However, this result can be equivalently interpreted as a bromide-deficient surface, an interpretation that shapes the way we think about charge trapping in these materials. One can assess the validity of each interpretation by considering existing *ab initio* calculations of $APbX_3$ surface defects. For a lead-rich surface, extra lead atoms on CsX facets would need to occupy sites such as adatoms, antisites, and interstitials, which have prohibitively high (>2 eV) formation energies.[64-66] Additionally, a lead-rich surface introduces defect levels that are too deep (defined here as $>5k_bT$) within the band gap to be consistent with 80-90% PLQY for as-synthesized $CsPbBr_3$ nanocrystals.[65] In contrast, a bromide-deficient surface would present bromide vacancies as the dominant defect type, which introduces shallow (defined here as $<5k_bT$) defect levels.[73-75] The

presence of surface bromide vacancies is also consistent with labile oleylammonium bromide ligand pairs, bromide-poor synthetic conditions, and high anionic conductivities.[76-79] Therefore, for both electronic and synthetic reasons, we believe that the 1:2.83±0.02 Pb:Br surface ratio can be accounted for with bromide vacancies rather than excess lead atoms.

3.2: The Role of Surface Halide Vacancies in Charge Trapping

Non-stoichiometric nanocrystal surfaces can harm optoelectronic performance by creating localized trap states.[60, 80-82] Guided by non-stoichiometric XPS results, halide-deficient surfaces were investigated as the potential source of charge trapping. We sought a method for controlling the introduction of halide vacancies on the surface of $CsPbX_3$ nanocrystals. Given the unstable nature of lead halide perovskite materials, it was particularly important to devise a method that can remove surface halides without altering or degrading the material in any other way. This was achieved by directly exploiting the weak bonding of oleylammonium halide ligand pairs, whose chemical equilibrium is described by equation 3.1. V_X represents a surface halide vacancy.

$$RNH_3{}^+X^- + CsPbX_3 \cdot V_X \leftrightarrow CsPbX_3 \cdot RNH_3{}^+X^- \tag{3.1}$$

It is unfavorable for oleylammonium ions to dissociate as discrete solvated ions in low polarity solvents such as toluene, therefore they are most likely removed from the surface with a counterion to preserve charge neutrality.[83] With oleate ions absent from the surface,[58, 62, 84] halide ions are the only available counterions present. A simple dilution experiment offers a very mild and controllable way to introduce surface halide vacancies as the ligand pair equilibrium shifts towards free species. As such, monitoring the PLQY over a range of concentrations offers direct insight into the PLQY dependency on the halide vacancy concentration. Although excessive dilution can induce rapid degradation of $CsPbX_3$ nanocrystals, this was only found to occur for nanocrystal concentrations <0.005 μM, which is far below the concentrations utilized here.

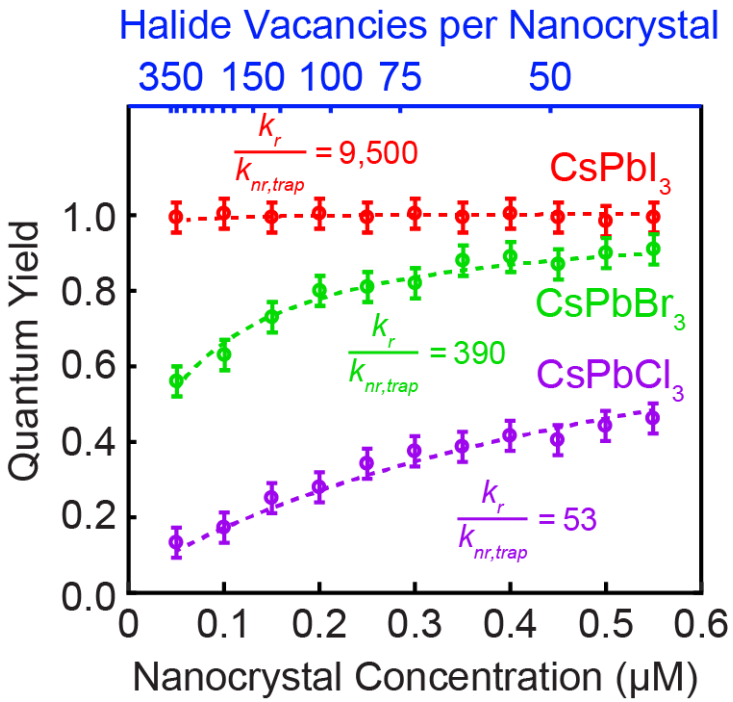

Figure 3.2: Absolute PLQY as a function of nanocrystal concentration for $CsPbCl_3$, $CsPbBr_3$, and $CsPbI_3$. Nanocrystal concentration and surface halide vacancy concentration are inversely related due to weak binding of oleylammonium halide ligand pairs. This allows the relationship between PLQY and halide vacancy concentration to be investigated. Surface halide vacancies are observed to have a negligible effect on $CsPbI_3$ nanocrystals, a moderate effect on $CsPbBr_3$ nanocrystals, and a significant effect on $CsPbCl_3$ nanocrystals. The data can be fit with a simple trapping model, which offers insight into the relative defect tolerance of each material by allowing the determination of $k_r/k_{nr,trap}$.

These experiments demonstrate a composition-dependent relationship between surface halide vacancy concentration and PLQY. Increasing the concentration of surface halide vacancies is observed to have a negligible effect on $CsPbI_3$, a small to moderate effect on $CsPbBr_3$, and a significant effect on $CsPbCl_3$, as shown in Figure 3.2. Although $CsPbI_3$ nanocrystal photophysics appear unchanged upon dilution, ^{1}H NMR spectroscopy experiments were used to confirm that dilution does in fact result in significant ligand pair desorption. The oleylammonium iodide ^{1}H NMR linewidth decreased significantly as the sample was diluted, as shown in Figure 3.3.

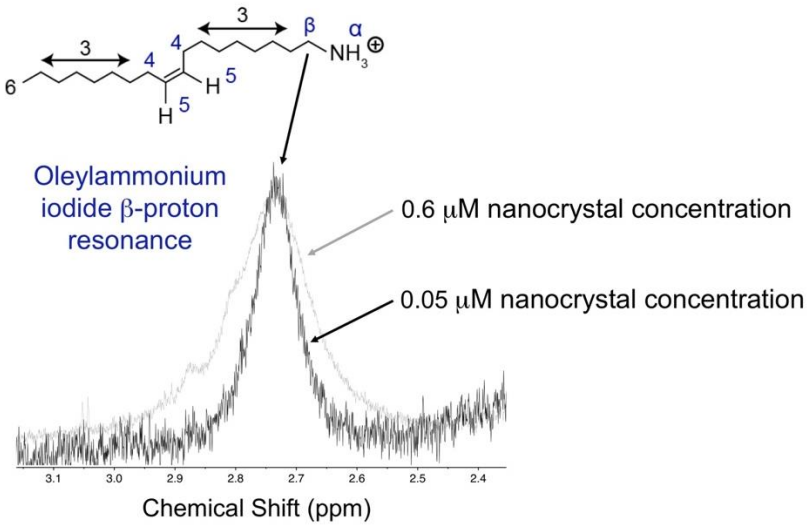

Figure 3.3: ^{1}H NMR of the oleylammonium iodide β-protons at the upper and lower bounds of the concentration used for the dilution experiment in Figure 3.2. The peaks are normalized to the same chemical shift and intensity so that their different linewidths can be directly visualized.

The linewidth of a ligand pair in fast exchange is a population-weighted average of free and bound signals,[85] as described by equation 3.2.

$$\lambda_{obs} = \frac{N_{free}}{N_{total}}\lambda_{free} + \frac{N_{bound}}{N_{total}}\lambda_{bound} \tag{3.2}$$

where λ is the linewidth and N is the number of ligand pairs per nanocrystal. N_{total}, λ_{free}, and λ_{bound} are unchanged by dilution, therefore a narrowing of the observed linewidth must be caused by a decrease in N_{bound} and a concomitant increase in N_{free}. This directly demonstrates that the equilibrium in equation 3.1 is shifting towards free species in these experiments. Figure 3.2 shows how this shift in equilibrium affects $CsPbCl_3$, $CsPbBr_3$, and $CsPbI_3$ nanocrystals.

Figure 3.2 was analyzed within the context of a simple trapping model, equations 3.3-3.4.

$$PLQY = 1 - \frac{N_{trap}}{\frac{k_r}{k_{nr,trap}} + N_{trap}}, \tag{3.3}$$

$$N_{trap} = \frac{N_{max}}{1+K_{eq}[RNH_3{}^{+}X^{-}]} \tag{3.4}$$

where k_r is the radiative rate, $k_{nr,trap}$ is the effective nonradiative rate per trap, N_{trap} is the number of surface traps per nanocrystal, N_{max} is the maximum number of surface traps per nanocrystal, K_{eq} is the free vs. bound equilibrium constant for oleylammonium halide ligand pairs, and $[RNH_3{}^{+}X^{-}]$ is the concentration of oleylammonium halide ligands pairs free in solution. N_{max} can be calculated from the nanocrystal size, and K_{eq} and $[RNH_3{}^{+}X^{-}]$ can be determined

experimentally via a binding isotherm collected by NMR spectroscopy. The results are shown in Figure 3.4. The determination of all variables other than k_r and $k_{nr,trap}$ leaves $k_r/k_{nr,trap}$ as the sole fitting parameter.

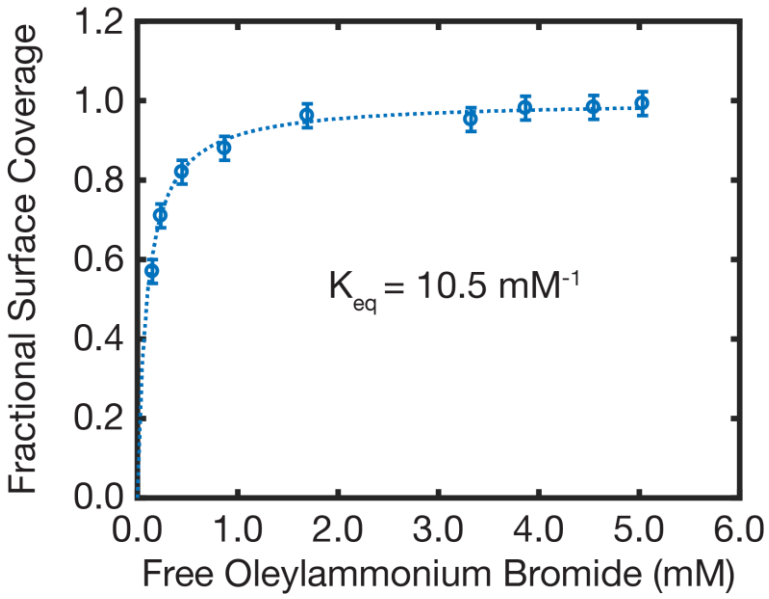

Figure 3.4: Binding isotherm for oleylammonium bromide ligand pairs on the surface of $CsPbBr_3$ nanocrystals. Data points were generated by analyzing the NMR linewidth of samples with variable ligand pair concentrations. The determination of the bound linewidth of oleylammonium bromide ligands allows one to convert the measured linewidth into free and bound fractions, which can then be converted to a fractional surface coverage. K_{eq} = 10.5 mM^{-1} is relatively low for nanocrystal capping ligands, consistent with the dynamic ligand shell of halide perovskites.[58]

Defect tolerance, which we define here as arising through very large values of $k_r/k_{nr,trap}$, varies significantly between the different halide compositions. This can be clearly observed in Figure 3.2. $k_r/k_{nr,trap}$ = 9,500 allows $CsPbI_3$ nanocrystals to maintain near-unity PLQY despite the presence of several hundred surface halide vacancies. Within the lead halide perovskite family, the iodide materials appear to be the closest to defect impervious. $k_r/k_{nr,trap}$ = 390 for $CsPbBr_3$ nanocrystals indicates these materials are also relatively tolerant of defects, although the effects of surface halide vacancies clearly cannot be ignored in this system. $k_r/k_{nr,trap}$ = 53 for $CsPbCl_3$ nanocrystals is the most analogous to defect-intolerant metal chalcogenide nanocrystals, where even a small number (<5% of the surface) of traps will yield PLQY values <20%. As a final comment in support of halide-deficient surfaces, it should be noted that if under-coordinated lead in a form other than that created by halide vacancies was the predominant source of charge trapping, no variation in $k_r/k_{nr,trap}$ and PLQY between different halide compositions would be expected. *Ab initio* calculations have shown that these defects form deep mid-gap states that would affect all halide compositions equally.[65]

3.3: *Ab Initio* Calculations of Halide-Deficient $CsPbX_3$ Surfaces

Ab initio calculations were used to further investigate halide-deficient surfaces as the suspected source of charge trapping. Specifically, density functional theory calculations were performed using the Vienna *ab initio* simulation package (VASP).[86] The core−valence interaction was described by the projector−augmented wave (PAW) method.[87] The cutoff for planewave expansion was set to 300 eV. Structures were relaxed until the force on each atom was smaller than 0.05 eV/Å. For the structural relaxation of systems with halide vacancies, the screened Coulomb hybrid functional of Heyd−Scuseria−Ernzerhof (HSE) was adopted,[88] and for the relaxation of other systems, the generalized gradient approximation of Perdew−Burke−Ernzerhof (GGA−PBE) was used.[89] The electronic structures for all systems considered were calculated at the HSE level after relaxation. The spin−orbit coupling (SOC) correction was also included in both structural relaxation and electronic structure calculations. The surface slab model was constructed based on orthorhombic $CsPbX_3$. It contains 11 atomic layers in a 2×2 supercell with 216 atoms. A vacuum layer larger than 12 Å was used to avoid interaction between periodic images. The Brillouin zone was sampled by the Γ point.

A single halide vacancy (V_{Cl}, V_{Br}, or V_I) was created on the surface of each crystal slab to model a halide-deficient surface. Native oleylammonium surface ligands are excluded because pristine $CsPbX_3$ crystals terminated by CsX facets exhibit fully delocalized, trap-free band structures without the need for passivating ligands, as shown previously in Figure 3.1. As such, differences in electronic structure between pristine and halide-deficient surfaces can be directly attributed to surface halide vacancies.

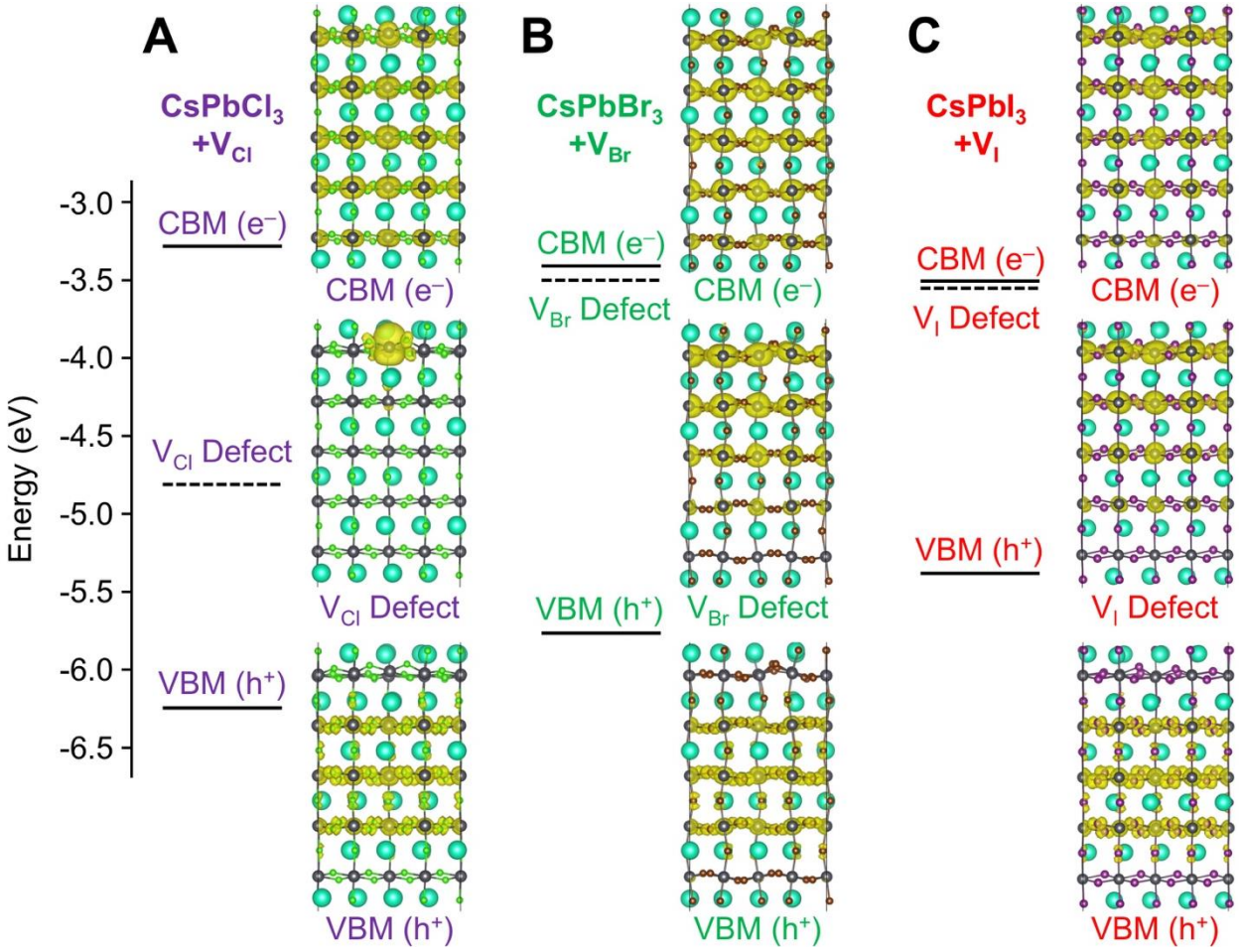

Figure 3.5: Electronic structure and charge density calculations at the HSE+SOC level of theory for (A) $CsPbCl_3$ with a surface chloride vacancy ($CsPbCl_3+V_{Cl}$), (B) $CsPbBr_3$ with a surface bromide vacancy ($CsPbBr_3+V_{Br}$), and (C) $CsPbI_3$ with a surface iodide vacancy ($CsPbI_3+V_I$). The top surface of the crystal slab is halide-deficient while the bottom surface is pristine. Absolute CBM energies are set according to electrochemically measured values,[90] and relative energies are given by the calculations. Cs, Pb, Cl, Br, and I atoms are shown as blue-green, gray, green, orange, and purple, respectively.

$CsPbCl_3+V_{Cl}$ is readily recognized as a three-level system, with a highly localized trap state deep within the band gap in addition to the fully delocalized valence band maximum (VBM) and conduction band minimum (CBM), as shown in Figure 3.5A. The mid-gap state exhibits significant atomic character; ~80% of this state is comprised of 6p orbitals of the lead atom that is left under-coordinated by the surface chloride vacancy. $CsPbBr_3+V_{Br}$ and $CsPbI_3+V_I$ also appear as three-level system, as shown in Figure 3.5B-C. However, the nature of the mid-gap defect levels differs significantly from the defect level in $CsPbCl_3+V_{Cl}$. Rather than being highly localized and deep within the band gap, these states are shallow and only weakly localized towards the halide-deficient surface. In these two systems, the under-coordinated lead atoms only contribute ~3% to the defect states. It should be noted that the HSE+SOC level of theory is required to observe the shallow levels in $CsPbBr_3+V_{Br}$ and $CsPbI_3+V_I$.[91, 92] Calculations with GGA–PBE+SOC, which

underestimated the band gap by ~1 eV,[93] produced nominally trap-free systems. However, sub-unity experimental PLQY values indicate that these systems are not trap-free.

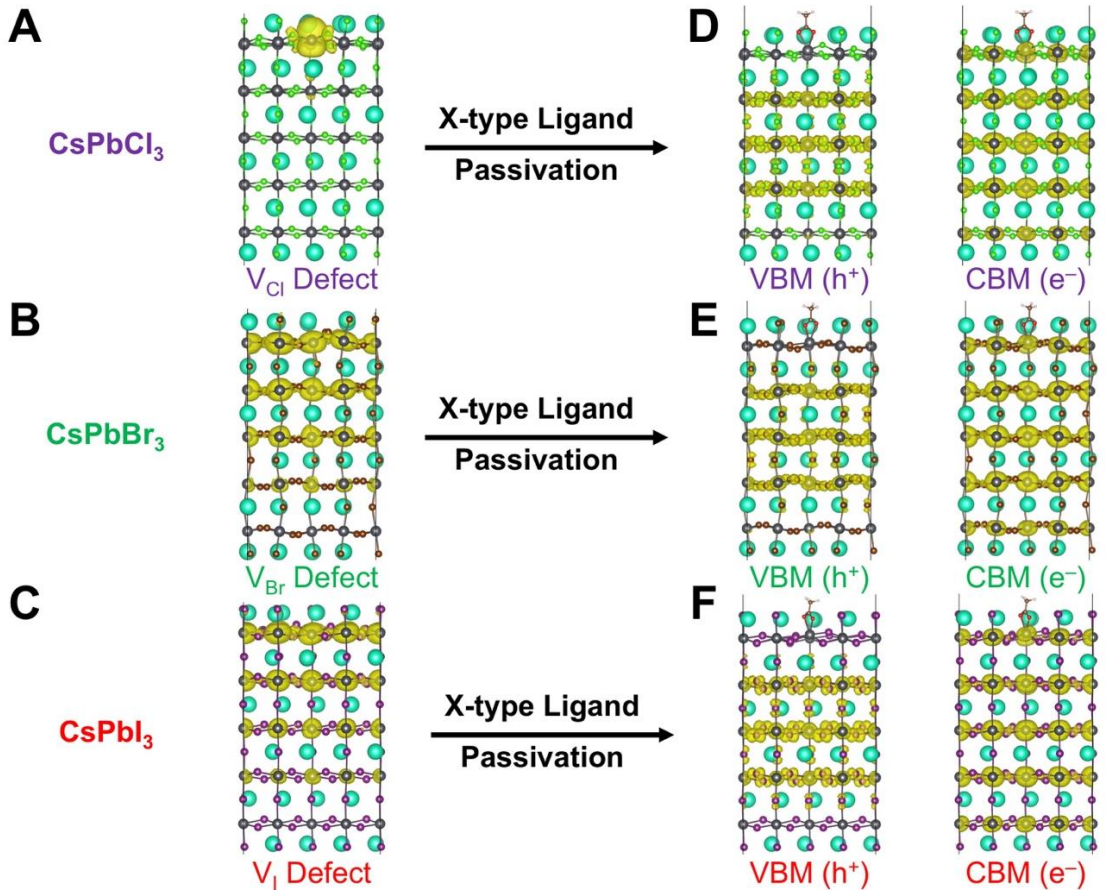

Figure 3.6: Charge density calculations at the HSE+SOC level of theory for (A) $CsPbCl_3$ with a surface chloride vacancy ($CsPbCl_3+V_{Cl}$), (B) $CsPbBr_3$ with a surface bromide vacancy ($CsPbBr_3+V_{Br}$), (C) $CsPbI_3$ with a surface iodide vacancy ($CsPbI_3+V_I$), (D) $CsPbCl_3+V_{Cl}$ from (A) with a CH_3COO^- X-type passivating ligand, (E) $CsPbBr_3+V_{Br}$ from (B) with a CH_3COO^- X-type passivating ligand, (F) $CsPbI_3+V_I$ from (C) with a CH_3COO^- X-type passivating ligand. VBM and CBM states are unaffected by surface halide vacancies in (A), (B), and (C), and thus are excluded. In all cases, X-type passivation of halide-deficient surfaces yields a trap-free band gap with fully delocalized VBM and CBM states. Cs, Pb, Cl, Br, I, O, C, and H atoms are shown as blue-green, gray, green, orange, purple, red, brown, and white, respectively.

It is particularly insightful to interpret these calculations of halide-deficient $CsPbX_3$ surfaces in light of experimental results. The calculated position of these defect levels relative to the CBM is highly consistent with the $k_r/k_{nr,trap}$ ratios determined in Figure 3.2. Nanocrystals can sustain a high charge transfer rate at high driving force,[94] and with the $CsPbCl_3+V_{Cl}$ defect state located directly in the middle of the band gap, efficient trapping of charges would be expected.[95] Additionally, the highly localized nature of this mid-gap state should result in significant nonradiative recombination, thereby yielding a relatively low $k_r/k_{nr,trap}$ as well as relatively poor PLQY values for $CsPbCl_3$ nanocrystals. In contrast to highly localized charges in $CsPbCl_3+V_{Cl}$,

these calculations suggest that electrons in halide-deficient $CsPbBr_3$ and $CsPbI_3$ are only weakly localized while holes remain fully delocalized, and thus trap-assisted nonradiative recombination is therefore expected to be relatively ineffective in $CsPbBr_3$ and $CsPbI_3$.[96-98] This allows $k_r/k_{nr,trap}$ to become quite large in these two systems, even though k_r is decreased relative to $CsPbCl_3$.[52, 99]

We sought to use *ab initio* calculations not only to investigate the predominant source of charge trapping, but also to identify a potential surface passivation mechanism. Oleate was investigated as a passivating ligand, as it has the potential to bind the under-coordinated lead atoms that have been implicated in charge trapping. X-type CH_3COO^- moieties, truncated computational models for oleate, were substituted into surface halide vacancies of the structures studied in Figure 3.5. These structures produce trap-free band gaps with fully delocalized VBM and CBM states for each halide composition, indicating that anionic surface ligands can effectively alter the energetics of lead-based defect levels, removing them from within the band gap. These results are summarized in Figure 3.6. However, several reports have demonstrated that oleate is not present on the surface of as-synthesized $CsPbBr_3$ nanocrystals,[58, 62, 84] which we ascribe to a hard-soft mismatch between hard carboxylates and soft lead binding sites.[22, 43] This motivates a search for new, softer ligands that can bind deleterious under-coordinated lead.

3.4: A Versatile Ligand Exchange and Purification Method

Investigations into the effects of new ligand shells would be greatly enhanced by a versatile ligand exchange method.[59, 100] However, to the best of our knowledge, no versatile colloidal ligand exchange method has yet been reported for $CsPbX_3$ nanocrystals. As such, precise manipulations of $CsPbX_3$ nanocrystal surfaces and entire ligand shells are not readily available. Here, we introduce a colloidal ligand exchange method that can exchange native oleylammonium halide ligand pairs for a mixture of alkylammonium halide and alkylammonium-alkylcarboxylate/alkylphosphonate ligand pairs, as depicted in Figure 3.7. This is accomplished by directly exploiting the weak bonding between native ligand pairs and the $CsPbX_3$ surface, which is directly demonstrated and quantified in Figure 3.8.

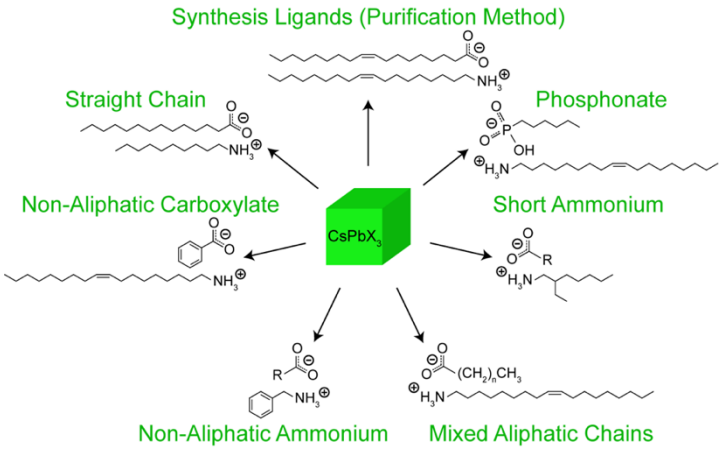

Figure 3.7: Schematic representation of the various ligand exchanges that can be performed using the method developed in this dissertation.

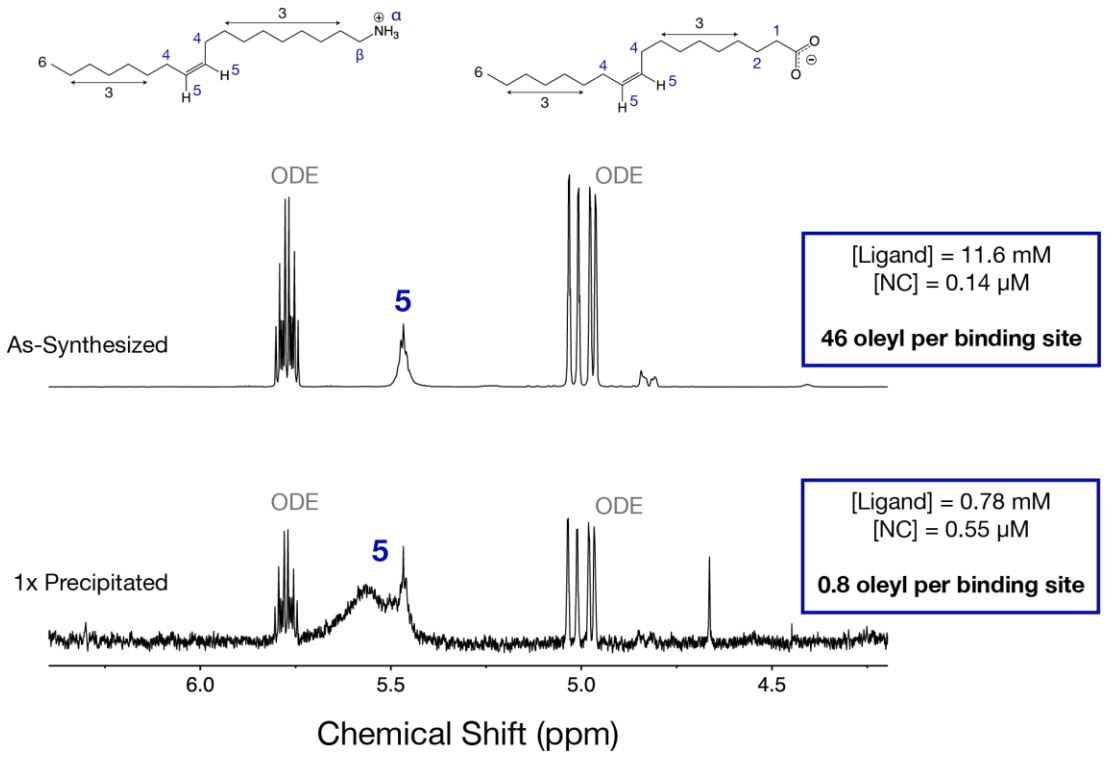

Figure 3.8: ^{1}H NMR spectra of an as-synthesized nanocrystal sample and a nanocrystal sample that was precipitated once and then resuspended in neat solvent. Quantitative ^{1}H NMR was used to investigate the surface ligand coverage before and after a precipitation and resuspension step. The majority of ligands are removed upon precipitation and resuspension, which enables the ligand exchange method developed here.

Stock solutions of nanocrystals (~1-2 μM) were precipitated with addition of an antisolvent (typically anhydrous ethyl acetate, 2× the volume of original nanocrystal solution), separated from the supernatant via centrifugation (10,000 rpm for 6 minutes), then resuspended in a dilute (~1-10 mM) mixture of new ligand pairs in anhydrous hexanes or toluene. Repeating this precipitation-resuspension process a total of 3 times was found to yield a complete exchange in all cases. Performing this process in neat solvent rather than a dilute ligand pair solution rapidly degrades the nanocrystals. Given the ionicity of perovskite nanocrystals, the use of molecular combinations that can form ion pairs is highly beneficial. Performing this exchange process on $CsPbBr_3$ nanocrystals with a dilute solution of alkylamine or alkylcarboxylic/alkylphosphonic acid alone, but not both species, yielded a weakly fluorescent, off-white precipitate. X-ray diffraction determined the precipitate to be comprised primarily of CsBr and Cs_4PbBr_6 phases, as detailed in Figure 3.9.

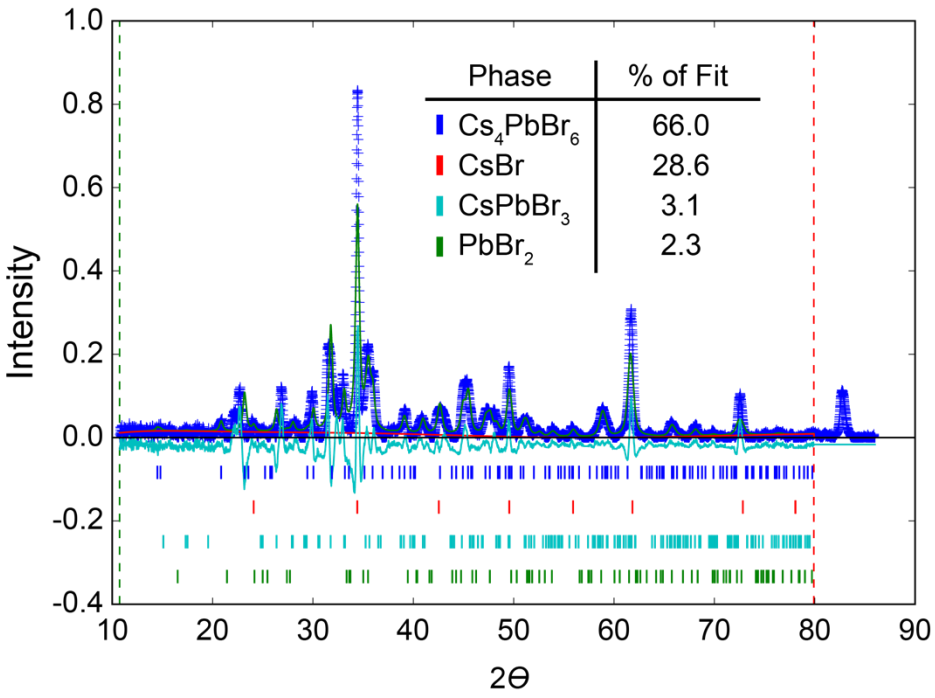

Figure 3.9: X-ray diffraction pattern of the off-white precipitate that forms when a ligand exchange is conducted on $CsPbBr_3$ nanocrystals using only amine or acid, but not both species. Only a small fraction (~3%) of nanocrystals are retained in the desired $CsPbBr_3$ phase, while the majority degrade into CsBr and Cs_4PbBr_6 phases. The contribution of each phase to the overall refinement is presented in the table.

To gain insight into the step-by-step evolution of this method, an exchange from as-synthesized, unsaturated ligand pairs (oleylammonium and oleate) to saturated ligand pairs (decylammonium and myristate) was studied via quantitative ^1H NMR for $CsPbBr_3$ nanocrystals, as shown in Figures 3.10 and 3.11.

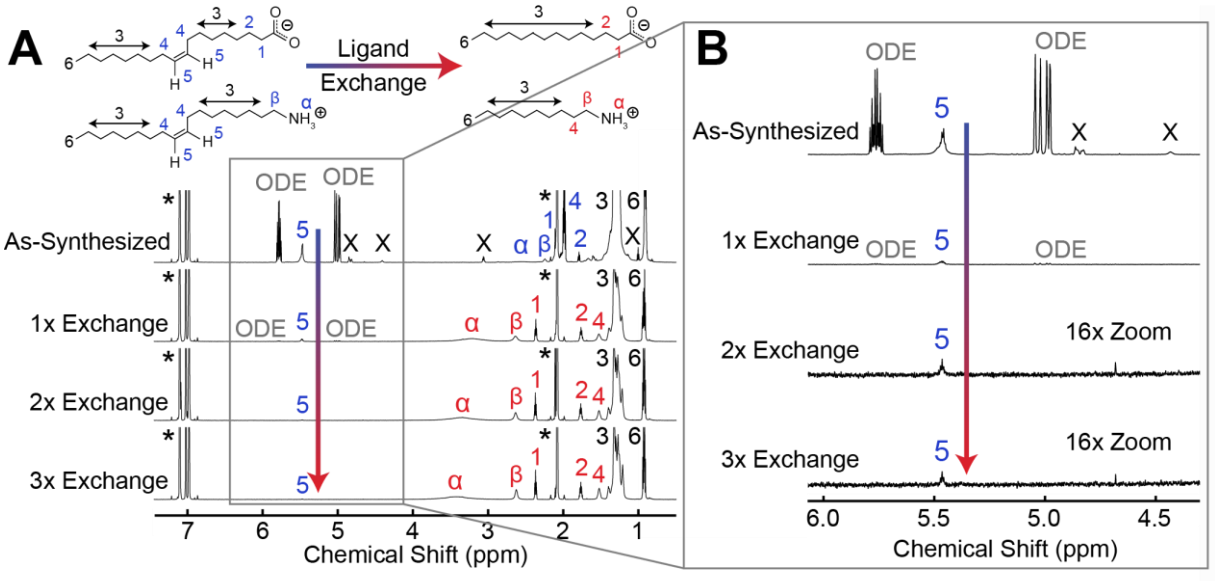

Figure 3.10: (A) ^{1}H NMR spectra for each step of a ligand exchange from native (blue) unsaturated ligand pairs (oleylammonium and oleate) to new (red) saturated ligand pairs (decylammonium and myristate). Resonances denoted by X are impurities. Concentration of $CsPbBr_3$ nanocrystals: 1.6 μM in toluene-d_8. (B) The 4-6 ppm region of interest from (A). This region contains resonances from native oleyl vinyl protons (**5**), 1-octadecene (**ODE**), and unknown impurities (**X**). All native species are reduced to <0.5% of their original concentration, demonstrating a complete ligand exchange.

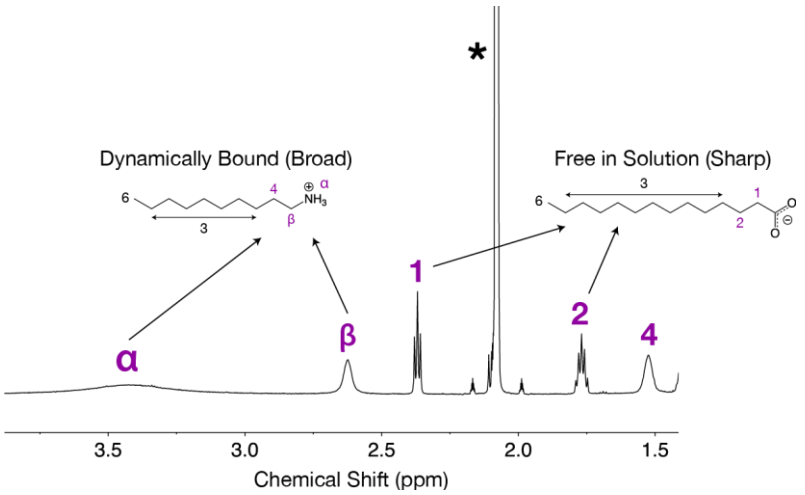

Figure 3.11: A closer look at the alkyl region of the ^{1}H NMR spectrum measured for a $CsPbBr_3$ nanocrystal sample 3x exchanged to decylammonium and myristate. Sharp peaks with the expected fine structure (a triplet and a quintet) are clearly observed for resonances **1** and **2** of myristate, characteristic of molecules rotating freely in solution. In contrast, resonances **α**, **β**, and **4** of decylammonium feature broad peaks without the expected fine structure, characteristic of molecules interacting with a nanocrystal surface. The broadening of resonances **4** and **β** are particularly illustrative given that the **α** resonance is also broadened by proton exchange. This reinforces observations from ourselves and others about long-chain, harder carboxylates like myristate and oleate tending to be absent from the ligand shell.

Unsaturated ligand pairs and 1-octadecene (ODE) both have alkene resonances in the 4-6 ppm range, which are useful for quantitative studies since they are located downfield from the many overlapping alkyl resonances in the 0-3 ppm region. Exchanging for saturated ligand pairs, which have no alkene resonances, allows the region of interest to be studied for the removal of alkene-containing species, all of which should be removed to constitute a complete ligand exchange and purification. These results are presented in Figure 3.10.

The exchange is observed to reach >99% exchange after three precipitation and resuspension steps, i.e. three exchange cycles. Appearance of decylammonium and myristate resonances and disappearance of alkene resonances confirms that native unsaturated ligand pairs are exchanged for non-native saturated ligand pairs, as shown in Figure 3.10. All native organic species being reduced to <0.5% of their original concentration confirms a complete ligand exchange. This is explicitly demonstrated by exchanging to ligand pairs such as benzylammonium-

oleate, oleylammonium-benzoate, and oleylammonium-difluoroacetate, which have spectrally isolated resonances that grow in downfield of the overlapping alkyl region as the exchange progresses. Figures 3.12-3.14 present a closer look at the key features of each exchange. Each of these resonances shows a broadened peak that is characteristic of interaction with nanocrystal surfaces.[33, 59, 94, 101]

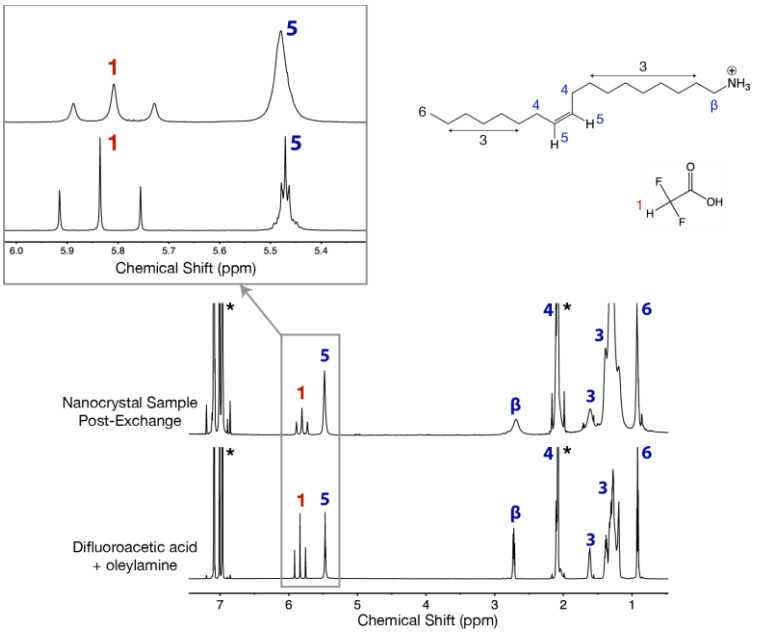

Figure 3.12: ^{1}H NMR spectrum of $CsPbBr_3$ nanocrystals 3x exchanged to difluoroacetate-oleylammonium ligand pairs, with a reference spectrum of the same ligand pair free in solution included below the nanocrystal sample. In the presence of nanocrystals, each species of the ligand pair displays broadened resonances, which are characteristic of interaction with the surface.

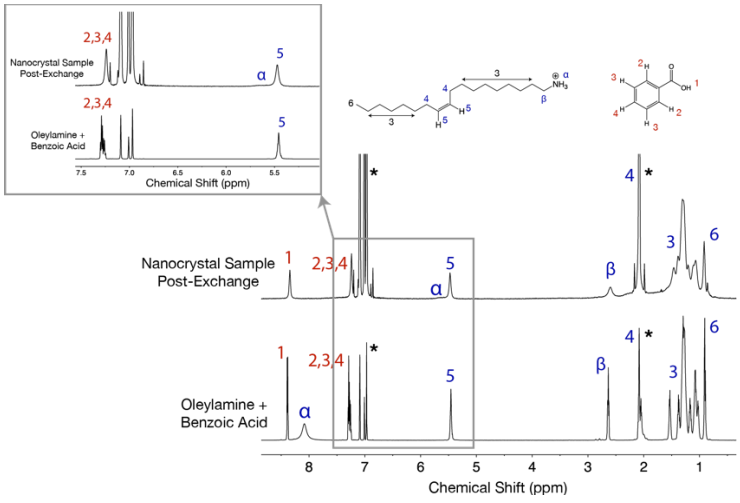

Figure 3.13: ^{1}H NMR spectrum of $CsPbBr_3$ nanocrystals 3x exchanged to benzoate-oleylammonium ligand pairs, with a reference spectrum of the same ligand pair free in solution included below the nanocrystal sample. In the presence of nanocrystals, each species of the ligand pair displays broadened resonances, which are characteristic of interaction with the surface.

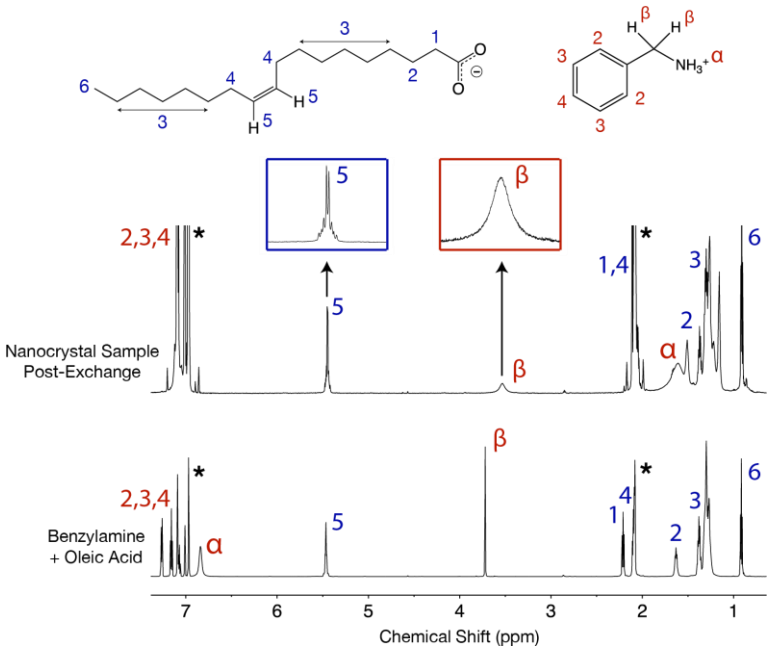

Figure 3.14: ^{1}H NMR spectrum of $CsPbBr_3$ nanocrystals 3x exchanged to benzylammonium-oleate ligand pairs, with a reference spectrum of the same ligand pair free in solution included below the nanocrystal sample. Resonance 5 from oleate shows no broadening, further supporting existing literature regarding the absence of oleate in the ligand shell. In contrast, the β resonance of benzylammonium broadens significantly when nanocrystals are present, indicating this molecule is acting as a capping ligand.

This exchange method also serves to purify nanocrystals of ODE, impurities, and synthesis byproducts such as lead oleate; the presence of these undesirable species was shown directly in Figure 2.4. As such, a resuspension solution of dilute oleylamine and oleic acid can be used to purify as-synthesized nanocrystals without compromising high PLQY or colloidal stability. Figure 3.15 presents X-ray diffraction, absorbance, photoluminescence, TEM, and integrating sphere PLQY measurements that confirm that the inorganic nanocrystalline core remains unchanged, indicating that purification induces no macroscopic changes to the ensemble of particles.

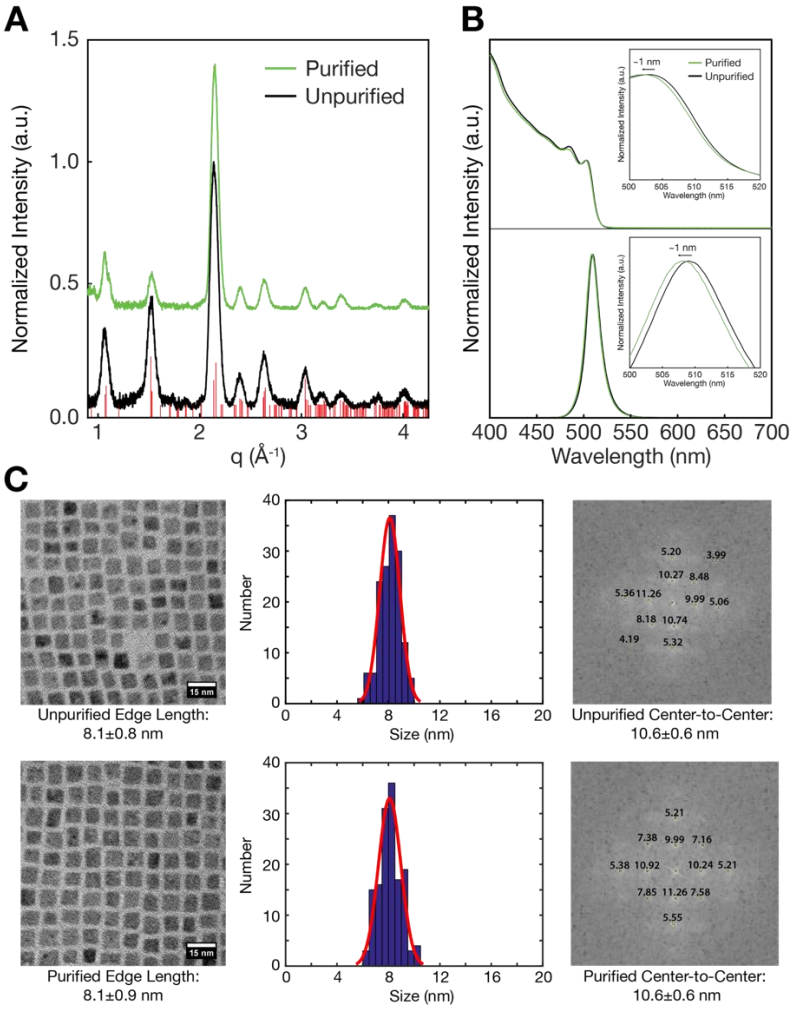

Figure 3.15: (A) X-ray diffraction patterns, (B) absorbance and fluorescence spectra, and (C) TEM images (left) with size distributions (middle) and interparticle spacing (right) of $CsPbBr_3$ nanocrystals before and after purification. Purification leaves nanocrystal size, shape, and ligand coverage virtually unchanged. For each image, 75 particles were measured for the histogram.

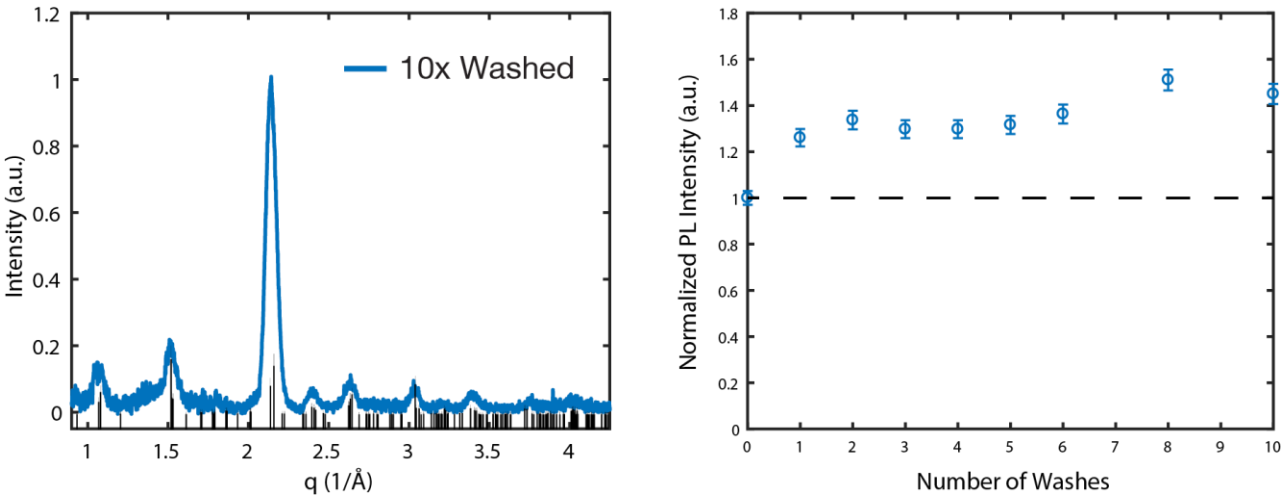

Figure 3.16: Demonstration of the benign nature of the purification process. XRD pattern of a sample washed 10× instead of the standard 3×, and PL intensity measured along each step of the same process. XRD shows the orthorhombic perovskite phase with no Cs_4PbBr_6 peaks present, indicating that the entire sample is preserved in the desired $CsPbBr_3$ phase. The PL intensity also behaves as expected. All samples were measured at identical nanocrystal concentration; thus, PL intensity is a direct reflection of PLQY. The initial removal of lead oleate increases PLQY, which then remains constant within measurement error for several more washes, and then starts to increase again for 8 and 10 washes. We attribute this final increase to the gradual loss of nanocrystals – resuspending slightly fewer nanocrystals in the same concentration of ligand throughout yields a slightly higher ligand:nanocrystal ratio, thus shifting the dynamic ligand equilibrium towards the surface.

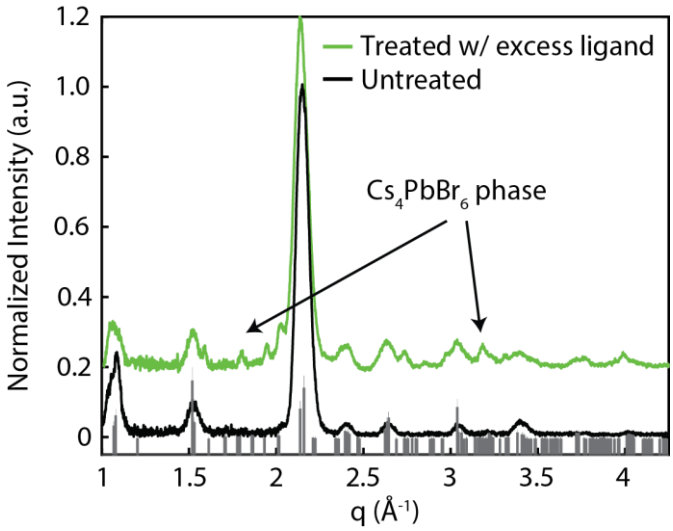

Figure 3.17: XRD pattern of an untreated sample (black) and a sample 3x treated (green) with an excess of oleylammonium-oleate pairs. Approximately 30 ion pairs per available nanocrystal binding site were used. Care must be taken to preserve the entire sample in the desired $CsPbBr_3$ phase. Treatment with an excess of ligand yields partial transformation to the Cs_4PbBr_6 phase, which is not surprising given the growing body of literature about ligand-mediated transformations between $CsPbBr_3$ and Cs_4PbBr_6 nanocrystals.[84, 102, 103]

3.5: Softer Lewis Bases Bind to Nanocrystal Surface

With control over entire ligand shells established, new passivating ligand pairs were investigated. In light of the proposed hard-soft mismatch between hard oleate and soft lead, softer carboxylates were targeted by exploring tail groups that decrease electron density on the binding head, as described in Figure 3.18 and Table 3. This can be accomplished through resonance and/or induction.[104, 105]

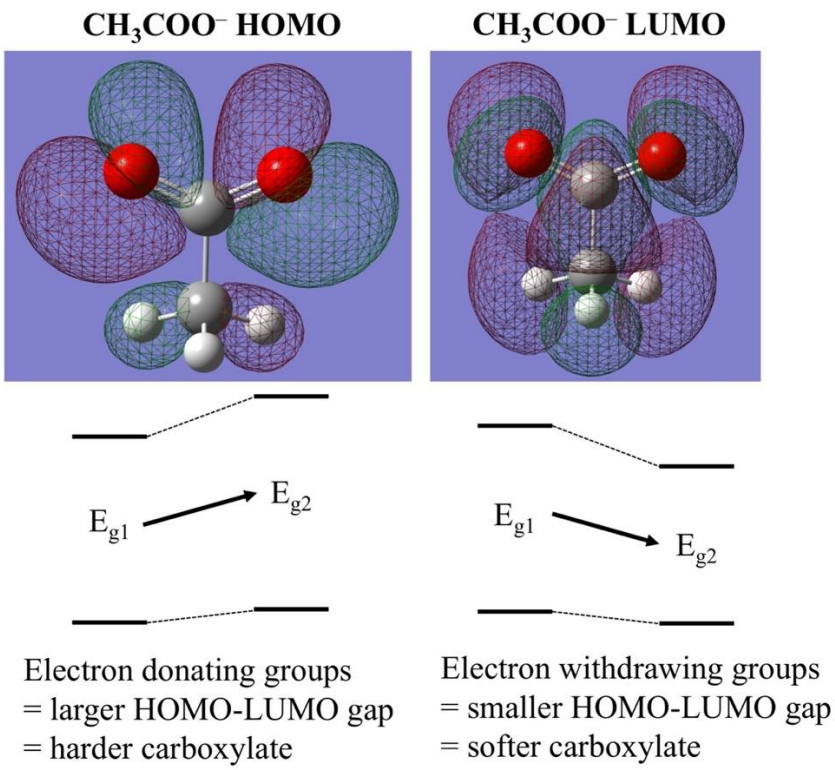

Figure 3.18: Density functional theory (DFT) calculations of the acetate anion. The HOMO is localized primarily on the O atoms of COO^-, while the LUMO is primarily on the C atom of COO^-. Because C is less electronegative than O, the LUMO energy will be changed more significantly by electron donating/withdrawing groups than will the HOMO. Electron donating groups are expected to increase the HOMO-LUMO gap by destabilizing the LUMO more than the HOMO, whereas electron withdrawing groups are expected to decrease the HOMO-LUMO gap by stabilizing the LUMO more than the HOMO. Smaller HOMO-LUMO gaps correspond to softer, more polarizable binding heads, thus we investigated new carboxylate with electron withdrawing tail groups, namely fluoroacetate, difluoroacetate, trifluoroacetate, and benzoate. DFT calculations confirm that these species have smaller HOMO-LUMO gaps than acetate, and thus are softer, as shown in Table S5. In contrast, an electron donating alkyl chain (e.g. for pentanoate) yields a larger HOMO-LUMO gap, and thus a harder carboxylate.

Table 3: HOMO-LUMO gap energies for various carboxylate anions

Anion	**HOMO-LUMO gap (eV)**
Acetate	11.07
Fluoroacetate	11.02
Difluoroacetate	10.78
Trifluoroacetate	10.47
Benzoate	7.40
Pentanoate	11.35

Following a ligand exchange to oleylammonium–R-COO$^-$ pairs, where R-COO$^-$ is benzoate, fluoroacetate, and difluoroacetate, Nuclear Overhauser Effect (NOESY) NMR spectroscopy confirms that these softer carboxylates bind to the nanocrystal together with oleylammonium, as shown in Figure 3.20A-B. Each ligand pair features negative (black) cross peaks in the presence of nanocrystals, in contrast to positive (red) cross peaks when no nanocrystals are present such as in Figure 3.19.[58, 106]

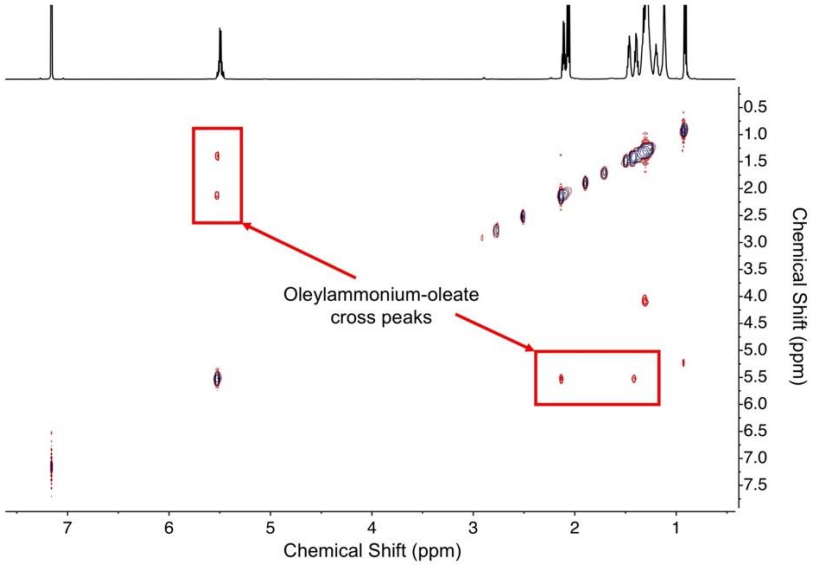

Figure 3.19: Example ^{1}H NOESY NMR spectrum of ligands pairs free in solution without the presence of nanocrystals. In this case, the ligand pair is oleylammonium-oleate. These species display positive (red) NOE signals, which is characteristic of the rapid tumbling of small molecules. This stands in contrast to the negative (black) NOE signals presented for the ligand pairs plus nanocrystals in the main text. This change in sign indicates that the tumbling frequency of ligand pairs decreases significantly in the presence of nanocrystals, thereby confirming their interaction with the nanocrystal surface.

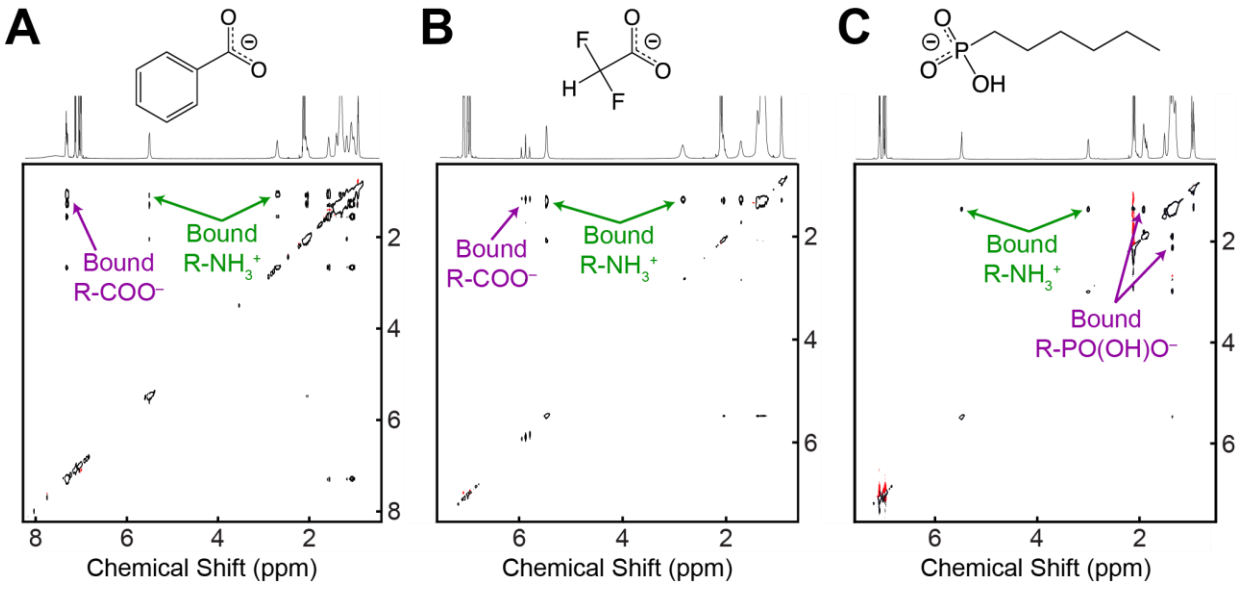

Figure 3.20: ^{1}H NOESY NMR spectra of $CsPbBr_3$ nanocrystal samples exchanged to ligand pairs of oleylammonium and (A) benzoate, (B) difluoroacetate, and (C) hexylphosphonate. All ligand pairs feature negative (black) NOE signals rather than positive (red) NOE signals, thereby corroborating their interaction with the nanocrystal surface. A small amount of red coloring is also present, but this is due to t1 noise rather than a positive NOE signal.

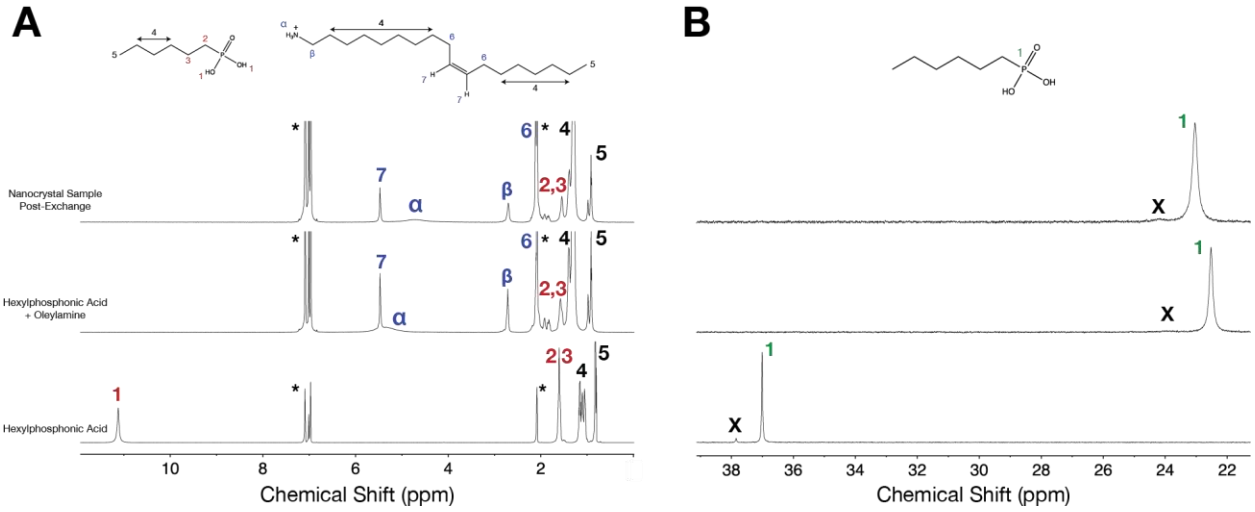

Figure 3.21: A) ^{1}H and B) ^{31}P NMR spectra of $CsPbBr_3$ nanocrystals 3x exchanged to oleylammonium-hexylphosphonate ligand pairs, with reference spectra of the same ligand pair free in solution included below the nanocrystal sample, along with reference spectra of hexylphosphonic acid alone. The ^{31}P provide strong evidence that hexylphosphonate is interacting with the nanocrystal surface, which we confirm with NOESY in the main text. As ion pairs are formed, hexylphosphonic acid is deprotonated, thus more electron density resides on the P atom of interest (green resonance 1). This is confirmed by the upfield shift in B). Additionally, some peak broadening occurs due to proton exchange, which is also consistent with ion pair formation. When the ion pair solution is used for a nanocrystal ligand exchange, the P resonance broadens considerably, consistent with binding to the nanocrystal surface. Finally, the phosphonate is expected to bind to surface Pb, which should shift some electron density off of the P atom due to the positive charge of Pb. ^{31}P NMR corroborates this, as the nanocrystal peak is shifted downfield from the ion pair peak, indicating less electron density is present on the P atom when these molecules are acting as nanocrystal capping ligands.

A change in the sign of the cross peak demonstrates that the tumbling frequency of these ligand pairs decreases significantly in the presence of nanocrystals, thereby confirming their interaction with the nanocrystal surface.[107] By utilizing the tail group to modulate electron density on the binding group, one can selectively coordinate or dissociate carboxylates in this system. The affinity of softer X-type ligands for the nanocrystal surface is further supported by the negative (black) NOE of oleylammonium-hexylphosphonate in Figure 3.20C, which corroborates binding of these ligand pairs.[108] Although X-type Lewis bases such as these could presumably also bind to surface cesium, this is thermodynamically unfavorable,[62] and therefore these new anionic ligands are likely binding entirely to surface lead by substituting into halide vacancies. Experimental evidence in support of this was provided by additional ^{1}H NMR and optical experiments (*vide infra*).

Analysis of the NMR linewidth of new surface-bound carboxylates provides valuable evidence for lead as the binding site for these ligands. Equation 3.2 can be rearranged to solve for the number of bound ligands:

$$N_{bound} = N_{total}\left(\frac{\lambda_{obs} - \lambda_{free}}{\lambda_{bound} - \lambda_{free}}\right) \tag{3.5}$$

By preparing purified samples at the upper limits of colloidal stability so that an initially saturated nanocrystal surface can be assumed, λ_{bound} was determined to be 290±30 Hz for protons directly adjacent to the binding head, as shown in Figure 3.22.

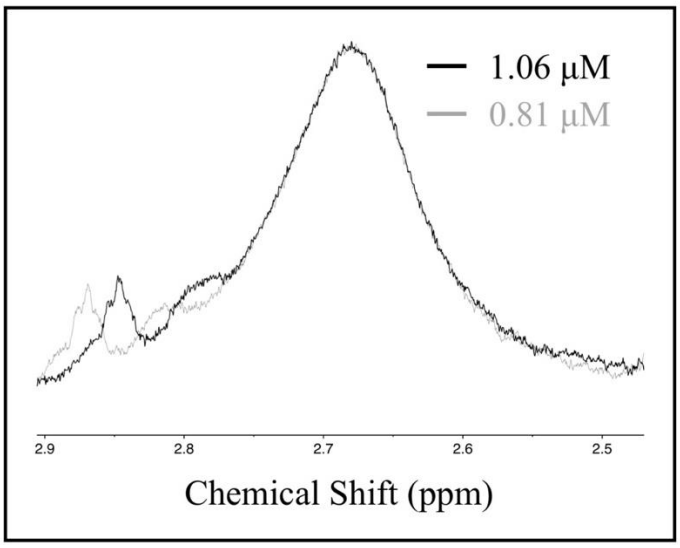

Figure 3.22: ^{1}H NMR of two different high concentrations of $CsPbBr_3$ nanocrystals and their native ligands, namely the oleylammonium bromide β-protons. The peaks are normalized to the same chemical shift and intensity so that their linewidths can be directly compared. The linewidth of a ligand in fast exchange is a population-weighted average of free and bound signals,[85] thus no measurable change in the NMR linewidth demonstrates that the ligand equilibrium remains unchanged in this high concentration region.

A saturated solution of the same nanocrystals following a ligand exchange to oleylammonium-difluoroacetate pairs displayed a linewidth of 10.7±0.2 Hz for the difluoroacetate proton, which corresponds to the formation of 180±20 new lead–difluoroacetate bonds for a fully passivated surface. The determination of 180±20 new bonds to lead is supported by the simple trapping model used in Figure 3.2. These $CsPbBr_3$ nanocrystals, which displayed a PLQY value of 62±3% before the ligand exchange, are expected to have 190±20 surface halide vacancies. These values indicate that new anionic X-type ligands access ~12% of the nanocrystal surface, which is in close agreement with a previous report from our group.[71] Specifically, these ligands must pack onto the planar surfaces of the cube, not its edge or corners, as can be seen in Figure 3.23.

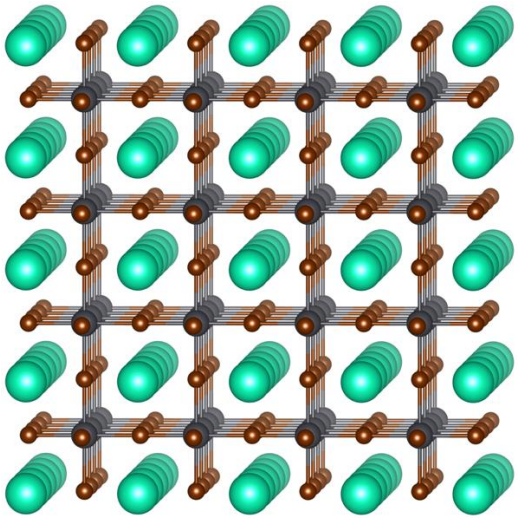

Figure 3.23: View of $CsPbBr_3$ crystal lattice with CsBr termination. Blue-green atoms are Cs, gray atoms are Pb, and orange atoms are Br. The enumeration of 190±20 traps per nanocrystal is nearly identical to that of the number of edge and corner atoms (188±10 per 9.4±0.5 nm nanocrystal), and it is well-known that edge and corner atoms are the most easily removed since they have the fewest neighbor interactions. However, for CsX termination, edges and corners are entirely Cs atoms, thus we conclude that this is simply a coincidence, and halide vacancies are present on the facets of the crystal.

3.6: Anionic X-type Ligands Can Produce Essentially Trap-Free Surfaces

Ab initio calculations suggested that formation of new lead–ligand bonds is expected to be accompanied by a significant increase in optoelectronic performance. As such, the effect of softer, X-type ligands on photoluminescence was investigated. Moderate 60-65% PLQY $CsPbBr_3$ nanocrystals were selected to maximize the presence of under-coordinated lead atoms. A fraction was exchanged with an oleylammonium-hexylphosphonate solution using the method described above, and a second fraction was purified with an oleylammonium-oleate solution of identical concentration as a control. Excited state lifetimes under 407 nm pulsed excitation are shown in Figure 3.24. Lifetime values were determined by fitting each decay curve to a single exponential over the first two decades.

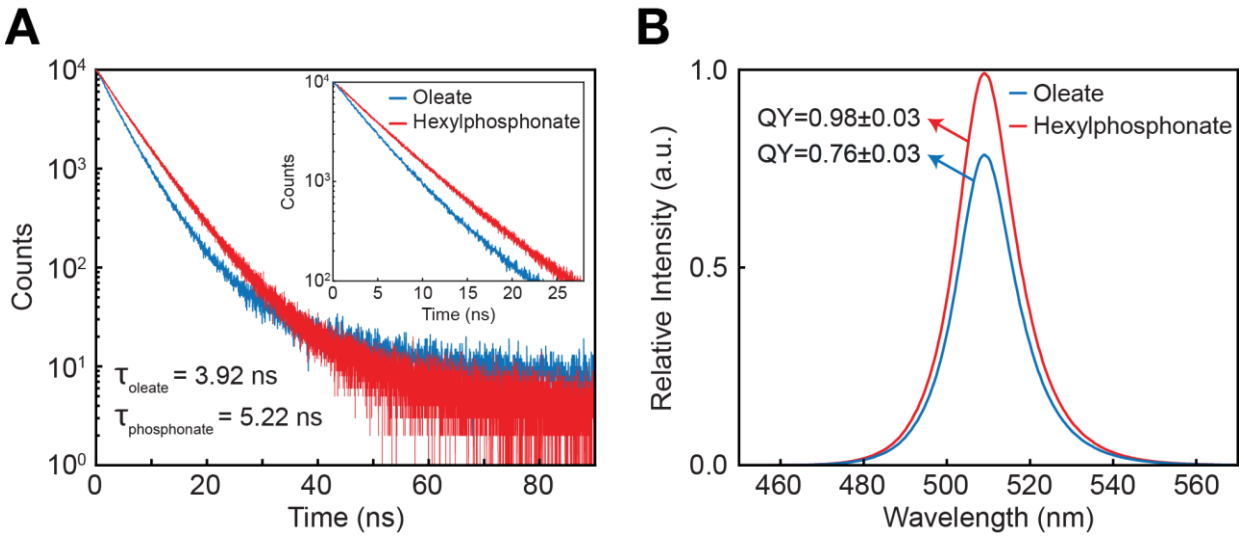

Figure 3.24: (A) Time-resolved photoluminescence lifetimes under pulsed 407.7 nm excitation (10 MHz) at room temperature for $CsPbBr_3$ nanocrystal samples in hexanes. Samples were exchanged to identical concentrations of oleylammonium-oleate (blue) and oleylammonium-hexylphosphonate (red). (B) Normalized steady-state photoluminescence spectra and absolute PLQY values for the same samples as in (A) under 437 nm excitation in hexanes. Nanocrystal and ligand pair concentration are identical for samples compared in (A) and (B), which is required for a meaningful PLQY comparison.

The purified oleylammonium-oleate sample (blue) shows a decay characteristic of an emitter with a distribution of trap states,[25, 36, 109-111] whereas the oleylammonium-hexylphosphonate exchanged sample (red) shows a decay that closely resembles that of a two-level emitter, indicating that deleterious trap states are almost completely passivated. Removal of trap states should be accompanied by a significant increase in PLQY, which was confirmed by integrating sphere measurements of PLQY=0.76±0.03 for oleylammonium-oleate (blue) and PLQY=0.98±0.03 for oleylammonium-hexylphosphonate (red), as shown in Figure 3.24B. Both samples were prepared with 4 ligand pairs per available binding site and measured at a nanocrystal concentration of 0.1 μM; identical nanocrystal and ligand pair concentrations are required for a meaningful PLQY comparison. Importantly, the demonstration of near-unity PLQY in $CsPbBr_3$ nanocrystals is not unique to hexylphosphonate. We demonstrate significantly improved photoluminescence with a wide variety of chemical functionalities, including fluorinated carboxylates, sulfonates, and phosphines as shown in Figures 3.25-3.27.

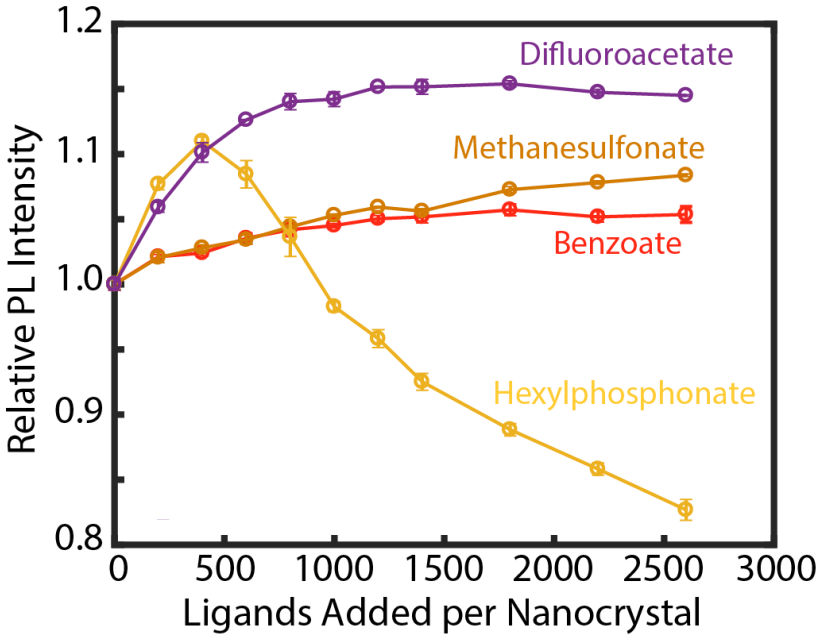

Figure 3.25: Comparison of the effect of various softer binding heads on $CsPbBr_3$ nanocrystal PL intensity. All ligand solutions were prepared with oleylammonium as a counterion. Ligand solutions were slowly titrated into cuvettes of dilute $CsPbBr_3$ nanocrystals, and PL was measured several times after each addition to ensure an equilibrium value. These results suggest that hexylphosphonate and difluoroacetate are the most effective for binding under-coordinated Pb atoms. In fact, Pb-phosphonate bond strengths can exceed those of the crystal cohesive energy, resulting in degradation of the nanocrystal when too much phosphonate is added, as observed here. However, so long as care is taken, near-unity PLQY $CsPbBr_3$ nanocrystals can be achieved, as was demonstrated in the main text.

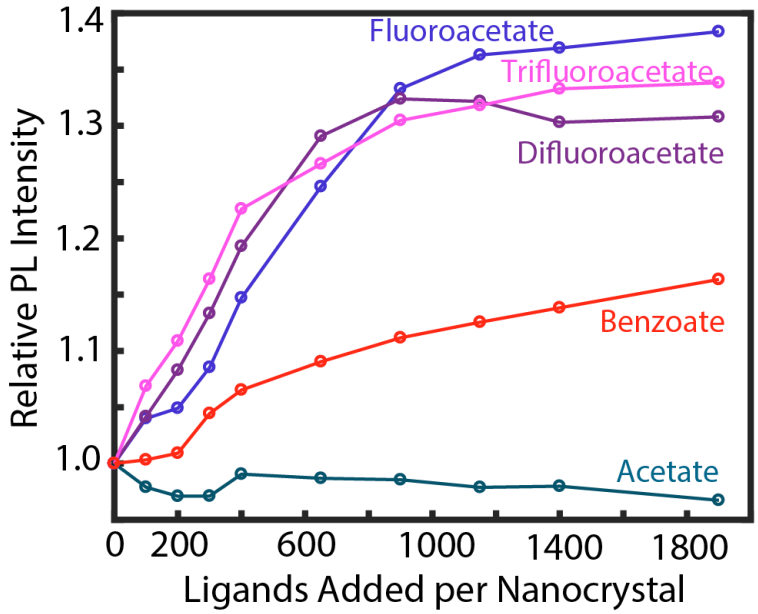

Figure 3.26: Comparison of the effect of carboxylates with variable softness binding heads on $CsPbBr_3$ nanocrystal PL intensity. All ligand solutions were prepared with oleylammonium as a counterion. Ligand solutions were slowly titrated into cuvettes of dilute $CsPbBr_3$ nanocrystals, and PL was measured several times after each addition to ensure an equilibrium value. Acetate, the hardest carboxylate in this experiment, has a negligible effect on PL, owing to the unfavorable hard-soft interaction between acetate and Pb. In contrast, benzoate and fluorinated carboxylates significantly improve PL, as these binding heads are softer and thus better suited to bind Pb. No clear trend is observed between the various fluorinated carboxylates. Although benzoate is the softest carboxylate present, the steric hindrance of the aromatic ring hinders its ability to substitute into halide vacancies, and thus PL cannot be improved as significantly as for other softer carboxylates. This highlights the importance of sterics in addition to the hard/soft match with lead.

We have focused entirely on the coordination chemistry between surface lead and passivating ligands to explain the coordination and dissociation of various species, but solubility may also play a role. For example, small fluorinated carboxylates will be less soluble in toluene than oleate and therefore could be driven to the surface by solubility effects rather than binding affinity for surface lead. To address this issue directly, a long chain analogue to difluoroacetic acid was synthesized, namely 2,2-difluorononanoic acid. In an optical comparison between oleylammonium-difluoroacetate and oleylammonium-2,2-difluorononanoate, both ligand pairs were observed to increase $CsPbBr_3$ PLQY by ~120%, as seen in Figure 3.27.

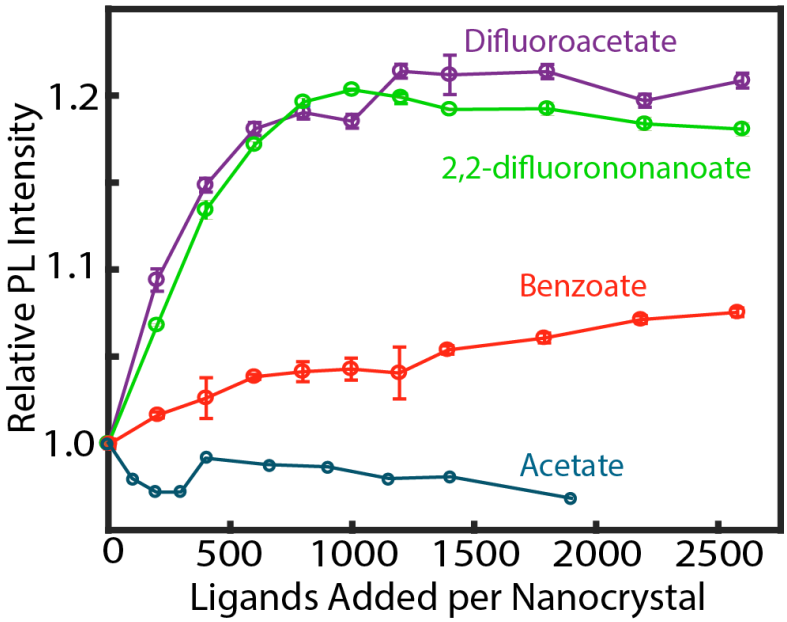

Figure 3.27: Comparison of the effect of carboxylates with variable steric hindrances on $CsPbBr_3$ nanocrystals relative PL. Given that these ligands are proposed to bond to under-coordinated Pb by substituting into halide vacancies, it is expected that sterics close to the binding head will play a significant role in surface passivation and thus PLQY. This is clearly observed with benzoate – although this is the softest carboxylate in the comparison, the steric bulk of the aromatic ring makes it difficult for this ligand to substitute into halide vacancies. Ligands such as difluoroacetate and 2,2-difluorononanoate have less steric hindrance near the binding head, and thus are more effective

for surface passivation. However, as the nanocrystal surface approaches saturation, the long alkyl chain of 2,2-difluorononanoate hinders the efficacy of this ligand, and thus it is not quite as effective as difluoroacetate.

No significant difference in surface passivation is observed at lower concentrations, indicating that solubility plays a minimal role. At higher concentrations, difluoroacetate yields a slightly higher PLQY, indicating that the long alkyl chain of 2,2-difluorononanoate hinders packing efficiency as coverage of the nanocrystal surface approaches saturation.

This demonstration of X-type ligand pairs as effective passivating ligands for $CsPbBr_3$ nanocrystals stands in contrast to metal chalcogenide nanocrystals, where Z-type ligands such as $Cd(O_2CR)_2$ have been shown to play a critical role in surface passivation.[21, 59] In our exploration of Z-type ligands for $CsPbBr_3$ nanocrystals, namely lead oleate, we observed a negative effect on PLQY that is consistent with our arguments about under-coordinated surface lead. These results are summarized in Figure 3.28.

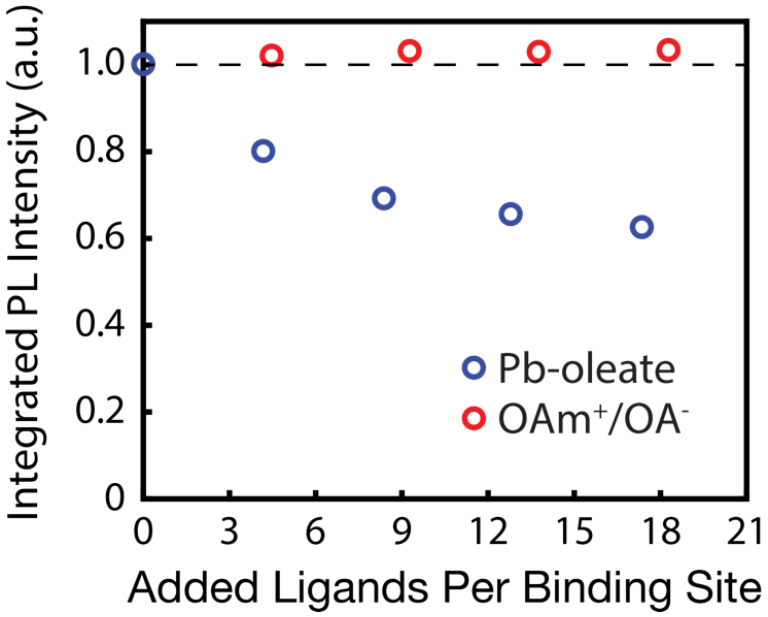

Figure 3.28: PL intensity of $CsPbBr_3$ nanocrystal samples (concentration 0.019 μM) titrated with solutions of lead oleate (blue) or oleylammonium-oleate (OAm^+-OA^-). Measurements were repeated several times over the course of hours to ensure no long-term degradation was occurring. Pb-oleate is a Z-type ligand, whereas oleylammonium-oleate is a pair of X-type ligands. Although Z-type ligands have been shown to be important for improving PLQY in metal chalcogenide nanocrystals, here they are observed to have a negative effect on $CsPbX_3$ nanocrystals. Pb-oleate represents a major byproduct of the synthesis given the Pb-rich conditions, further highlighting the need for a purification method that can remove this byproduct. This also has implications for the anion exchange of $CsPbX_3$ NCs. Typically, a PbX_2 salt is dissolved by oleylamine and oleic acid in toluene, and this solution is then added to a solution of nanocrystals to initiate the anion exchange. This means that Pb-oleate is present in significant concentrations, thus PLQY is almost certainly being harmed. The pursuit of anion exchange methods free from Pb-oleate, or free of Pb

in general, seem like worthwhile pursuits, although using our method, samples can be anion exchanged and then cleaned of all excess exchange solution.

Although this is not an exhaustive study of $CsPbX_3$ Z-type ligands, this result indicates that while the well-developed toolbox for metal chalcogenide nanocrystals can be readily applied to $CsPbX_3$ nanocrystals, differences in the nature of the bonding dictate different surface modification strategies.

3.7: A General Mechanism for $CsPbX_3$ Surface Passivation

$CsPbX_3$ nanocrystals spontaneously move towards simple cubic shapes with nearly perfect low-index CsX facets, which *ab initio* calculations reveal to be more favorable for PLQY than the alternative of PbX_2 facet termination.

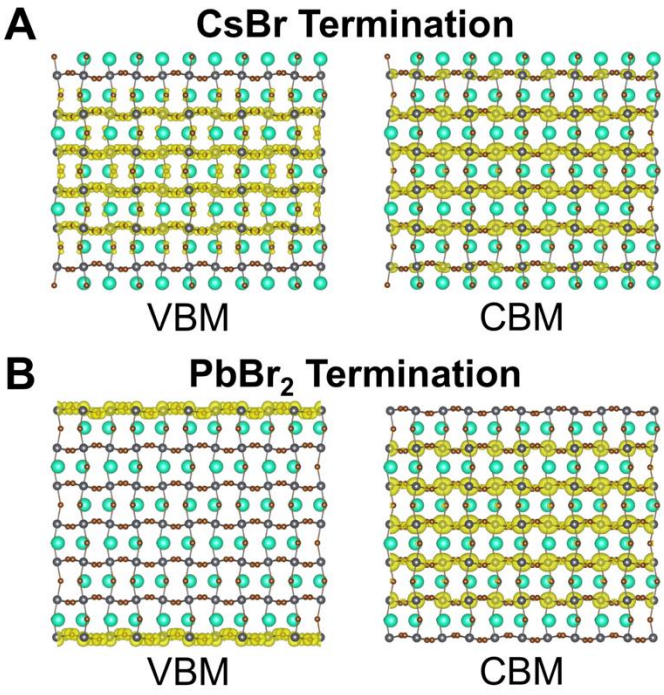

Figure 3.29: Charge density plots of the valence band maximum (VBM) and conduction band minimum (CBM) of (A) CsBr and (B) $PbBr_2$ surface terminations of $CsPbBr_3$ crystals. Blue-green atoms are Cs, gray atoms are Pb, and orange atoms are Br. CsBr termination yields a fully delocalized electronic structure that is expected for pristine semiconductor materials, whereas $PbBr_2$ termination yields a highly localized valence band maximum (VBM) that would introduce significant surface trapping. These results suggest that AX termination is highly beneficial for optoelectronic performance, and thus it is fortunate that these materials tend to spontaneously terminate with these facets.

The healing of point defects on these surfaces is essential for the realization of trap-free $CsPbX_3$ nanocrystals. Despite a growing body of literature on surface passivation of lead halide perovskite materials, a general understanding that can unify these reports does not yet exist. We propose that these findings can all be explained by the mechanism we present here. Lewis bases,

which can be ionic halide sources such as quaternary ammonium bromide salts or CH_3NH_3Br,[112, 113] neutral molecules such as thiophene or pyridine,[114] or anionic X-type ligands such as alkylphosphonates or S^{2-},[115, 116] substitute into surface halide vacancies and bind under-coordinated lead. These ligands raise the energy of lead 6p states to where they are no longer energetically accessible by photoexcited electrons in the conduction band, thereby increasing optoelectronic performance. This general surface passivation mechanism is depicted schematically in Figure 3.30.

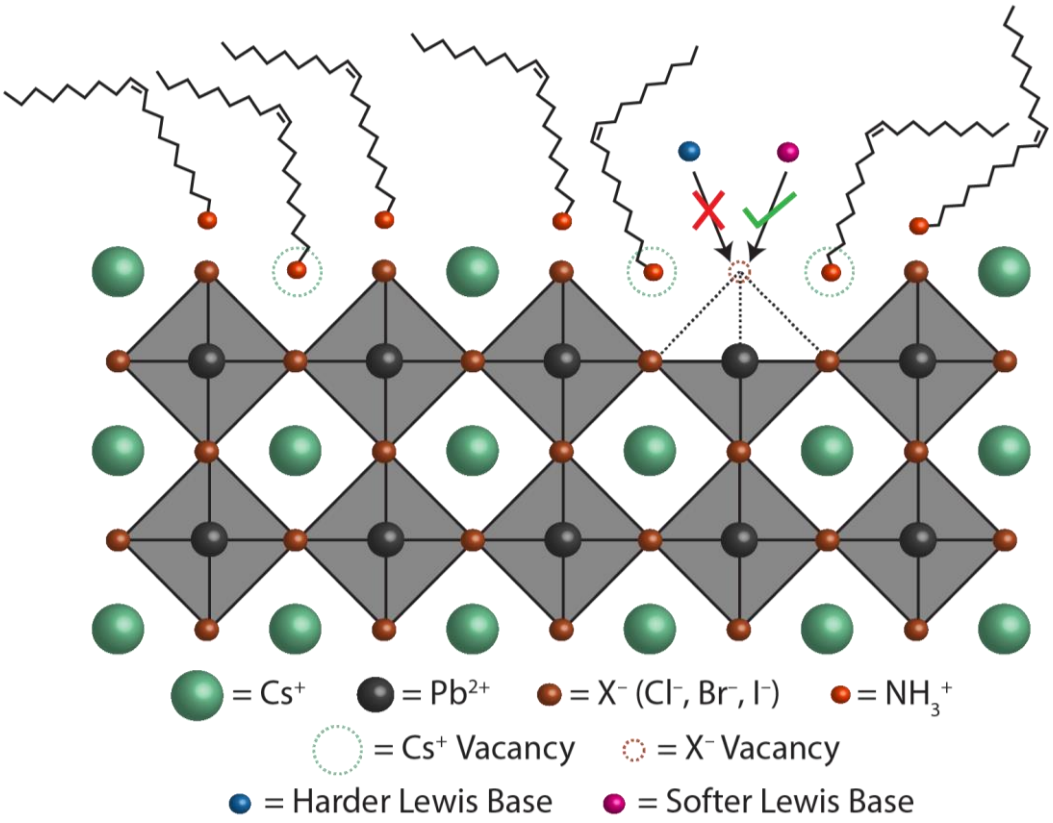

Figure 3.30: Schematic representation of a cesium- and halide-deficient surface terminated by CsX facets, consistent with experimental results. Approximately half of surface cesium is substituted by oleylammonium ions, and ~12% of surface halide sites are vacant. Halide vacancies create under-coordinated lead atoms, which can either be left unpassivated or passivated depending on the hardness or softness of the Lewis base that is available to coordinate lead.

The crystal terminates with the CsX facet, with both cesium and halide vacancies present. Halide vacancies expose underlying lead atoms, which can be unpassivated or passivated depending on the hardness of softness of the X-type Lewis base that is present.

3.8: Proposed Design Principles for Trap-Free $CsPbX_3$ Nanocrystals

Knowledge of $CsPbX_3$ surface chemistry and its role in charge trapping can be used to propose design principles for the preparation of trap-free $CsPbX_3$ nanocrystals. With strong

evidence for surface halide vacancies as the predominant source of charge trapping, design principles should focus on eliminating the presence and/or effects of these defects.

Table 4: Effect of various chemical functionalities on $CsPbX_3$ nanocrystal PLQY[a]

Significant Improvement of PLQY	**Negligible/Negative Effect on PLQY**
Hexylphosphonate (oleylammonium)	Oleate (oleylammonium)
Benzoate (oleylammonium)	Butyrate (oleylammonium)
Fluoroacetate (oleylammonium)	Acetate (oleylammonium)
Difluoroacetate (oleylammonium)	Carbonate (cesium)
Trifluoroacetate (oleylammonium)	Nitrate (lead)
2,2-difluorononanoate (oleylammonium)	Hydroxide (lead)
Methanesulfonate (oleylammonium)	Acetate (cesium)
Trioctylphosphine (none)	Lead oleate (none)

[a]The corresponding counterion (if applicable) for the chemical functionality of interest is shown in parentheses. Ion pairs with oleylammonium as the counterion were prepared as stoichiometric mixtures of organic acid and oleylamine at room temperature; lead oleate was synthesized at an elevated temperature before use; trioctylphosphine, cesium carbonate, lead nitrate, lead hydroxide, and cesium acetate were used as purchased.

Synthetic control over the surface halide vacancy concentration can be achieved by exploring alternative precursors to lead halide salts, which are intrinsically halide-deficient relative to the final $CsPbX_3$ nanocrystalline product. We find a recent report that decouples lead and halide stoichiometry by employing benzoyl halide precursors to be particularly promising.[117] When synthesizing $CsPbCl_3$, weak (PLQY <10%) luminescence was observed for a stoichiometric injection of chloride precursor, which stands in stark contrast to a record high PLQY of ~65% when an excess of chloride precursor was injected. XPS determined the highest X:Pb ratio for the product of this synthesis, suggesting that excess halide precursor can increase PLQY by minimizing surface halide vacancy concentrations.[118] From a post-synthetic perspective, we have demonstrated the importance of coordination chemistry in designing the optimal passivating ligand shell for $CsPbX_3$ nanocrystals. Under-coordinated lead atoms are the predominant source of charge trapping, and with lead as a relatively soft Lewis acid, the hardness or softness of Lewis bases must also be considered. Harder species such as alkylcarboxylates, carbonates, and nitrates are ineffective passivating ligands, while softer species such as alkylphosphonates, fluorinated carboxylates, and sulfonates were found to be effective passivating ligands, as summarized in Table 4 with the relevant counterion in parentheses. In summary, synthetic design of trap-free $CsPbX_3$ nanocrystals should include decoupled tunability of cesium, lead, and halide precursors, and post-synthetic design of ligand shells should employ ionic X-type Lewis acid-base pairs, where the softness of the Lewis base is well-matched to the softness of under-coordinated lead in the nanocrystal.

While the work presented here has focused entirely on $CsPbX_3$ nanocubes, we expect these findings to extend to nanoplates, nanowires, and other morphologies. Indeed, experiments on nanoplates and nanowires demonstrate similar trends, namely PLQY that is lowest in $CsPbCl_3$ and highest in $CsPbI_3$, as well as significant increases in PLQY of $CsPbBr_3$ materials when softer, X-type Lewis bases are employed, as shown in Figure 3.31.

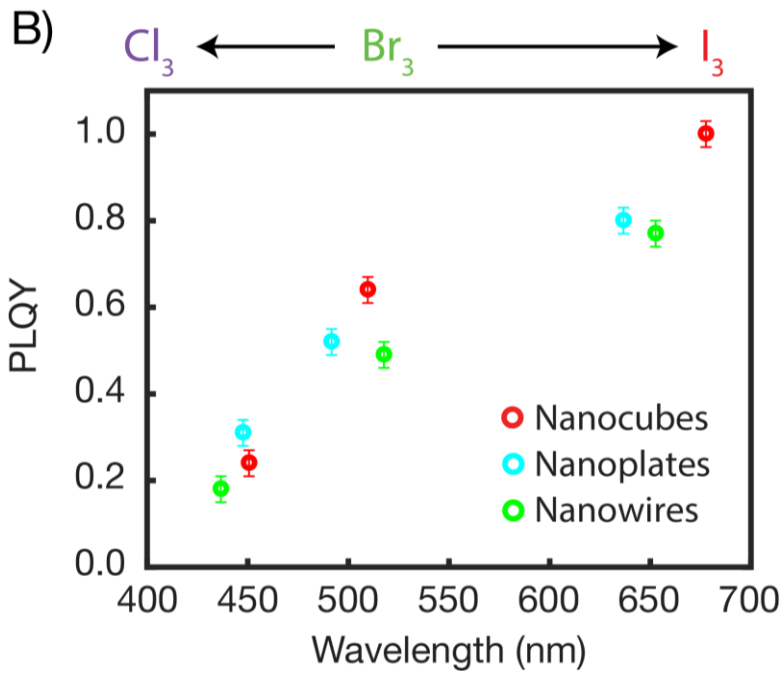

Figure 3.31: Comparison of PLQY as a function of halide composition for $CsPbX_3$ nanocubes, nanowires, and nanoplates. $CsPbBr_3$ samples were synthesized directly, and then anion exchanged to produce $CsPbI_3$ and $CsPbBr_{1.5}Cl_{1.5}$ nanomaterials. Nanowires and nanoplates exhibit the same trends as nanocubes, namely PLQY that is lowest in $CsPbCl_3$ and highest in $CsPbI_3$. As such, the general passivation mechanism is expected to readily extend to all morphologies, not just nanocubes.

This work provides a rational framework for highly luminescent lead halide perovskite nanocrystals of variable compositions and dimensionalities, which we anticipate will increase the performance of these materials in photonic and optoelectronic applications.

Chapter 4. Concluding Remarks and Outlook

We have developed a systematic route to highly luminescent $CsPbX_3$ nanocrystals by carefully investigating their surface chemistry through a combined experimental and theoretical study. Strong evidence was presented for surface halide vacancies as the predominant source of charge trapping. The number of trap states was quantified by ^1H NMR spectroscopy and is broadly consistent with a simple trapping model. Trap depth varies with halide composition, thus explaining the relatively low PLQY of $CsPbCl_3$ along with the high PLQY of $CsPbBr_3$ and $CsPbI_3$. We utilized hard-soft acid base theory to develop a general X-type ligand passivation scheme that is grounded in established principles of coordination chemistry, and we showed that the tail group of carboxylates can be used to selectively coordinate or dissociate these ligands. We used these findings to prepare essentially trap-free $CsPbBr_3$ and $CsPbI_3$ nanocrystals, and although we were unable to produce near-unity PLQY $CsPbCl_3$, we identified several promising routes to be pursued. Our findings are able to unify a wide variety of reports on improved luminescence in $CsPbX_3$ materials, thereby establishing a general mechanism for the passivation of lead halide perovskite surfaces. This work not only informs future post-synthetic efforts, but synthetic efforts as well. By providing both a general passivation mechanism and the ligand exchange tools required for precise manipulations of the surface, this work opens the door to future surface investigations as well as rational improvements of photonic and optoelectronic applications based on lead halide perovskite materials.

Bibliography

1. Rossetti, R.; Nakahara, S.; Brus, L. E., Quantum size effects in the redox potentials, resonance Raman spectra, and electronic spectra of CdS crystallites in aqueous solution. *J. Chem. Phys.* **1983,** *79* (2), 1086-1088.

2. Chestnoy, N.; Hull, R.; Brus, L. E., Higher excited electronic states in clusters of ZnSe, CdSe, and ZnS: Spin-orbit, vibronic, and relaxation phenomena. *J. Chem. Phys.* **1986,** *85* (4), 2237-2242.

3. Brus, L., Quantum crystallites and nonlinear optics. *Appl. Phys. A* **1991,** *53* (6), 465-474.

4. Vossmeyer, T.; Katsikas, L.; Giersig, M.; Popovic, I. G.; Diesner, K.; Chemseddine, A.; Eychmueller, A.; Weller, H., CdS Nanoclusters: Synthesis, Characterization, Size Dependent Oscillator Strength, Temperature Shift of the Excitonic Transition Energy, and Reversible Absorbance Shift. *The Journal of Physical Chemistry* **1994,** *98* (31), 7665-7673.

5. Colvin, V. L.; Alivisatos, A. P.; Tobin, J. G., Valence-band photoemission from a quantum-dot system. *Phys. Rev. Lett.* **1991,** *66* (21), 2786-2789.

6. Goldstein, A. N.; Echer, C. M.; Alivisatos, A. P., Melting in Semiconductor Nanocrystals. *Science* **1992,** *256* (5062), 1425.

7. Tolbert, S. H.; Alivisatos, A. P., High-Pressure Structural Transformations in Semiconductor Nanocrystals. *Annu. Rev. Phys. Chem.* **1995,** *46* (1), 595-626.

8. Murray, C. B.; Norris, D. J.; Bawendi, M. G., Synthesis and characterization of nearly monodisperse CdE (E = sulfur, selenium, tellurium) semiconductor nanocrystallites. *J. Am. Chem. Soc.* **1993,** *115* (19), 8706-8715.

9. Imran, M.; Ijaz, P.; Baranov, D.; Goldoni, L.; Petralanda, U.; Akkerman, Q.; Abdelhady, A. L.; Prato, M.; Bianchini, P.; Infante, I.; Manna, L., Shape-Pure, Nearly Monodispersed $CsPbBr_3$ Nanocubes Prepared Using Secondary Aliphatic Amines. *Nano Lett.* **2018,** *18* (12), 7822-7831.

10. Weidman, M. C.; Beck, M. E.; Hoffman, R. S.; Prins, F.; Tisdale, W. A., Monodisperse, Air-Stable PbS Nanocrystals via Precursor Stoichiometry Control. *ACS Nano* **2014,** *8* (6), 6363-6371.

11. Peng, X.; Wickham, J.; Alivisatos, A. P., Kinetics of II-VI and III-V Colloidal Semiconductor Nanocrystal Growth: "Focusing" of Size Distributions. *J. Am. Chem. Soc.* **1998,** *120* (21), 5343-5344.

12. Chen, Y.; Johnson, E.; Peng, X., Formation of Monodisperse and Shape-Controlled MnO Nanocrystals in Non-Injection Synthesis: Self-Focusing via Ripening. *J. Am. Chem. Soc.* **2007,** *129* (35), 10937-10947.

13. Hendricks, M. P.; Campos, M. P.; Cleveland, G. T.; Jen-La Plante, I.; Owen, J. S., A tunable library of substituted thiourea precursors to metal sulfide nanocrystals. *Science* **2015,** *348* (6240), 1226.

14. Kim, B. H.; Heo, J.; Kim, S.; Reboul, C. F.; Chun, H.; Kang, D.; Bae, H.; Hyun, H.; Lim, J.; Lee, H.; Han, B.; Hyeon, T.; Alivisatos, A. P.; Ercius, P.; Elmlund, H.; Park, J., Critical differences in 3D atomic structure of individual ligand-protected nanocrystals in solution. *Science* **2020,** *368* (6486), 60.

15. Hoffmann, R., How Chemistry and Physics Meet in the Solid State. *Angewandte Chemie International Edition in English* **1987,** *26* (9), 846-878.

16. Jahn, H. A.; Teller, E.; Donnan, F. G., Stability of polyatomic molecules in degenerate electronic states - I—Orbital degeneracy. *Proceedings of the Royal Society of London. Series A - Mathematical and Physical Sciences* **1937,** *161* (905), 220-235.

17. Alivisatos, A. P., Semiconductor Clusters, Nanocrystals, and Quantum Dots. *Science* **1996,** *271* (5251), 933.

18. Fukui, K.; Yonezawa, T.; Shingu, H., A Molecular Orbital Theory of Reactivity in Aromatic Hydrocarbons. *J. Chem. Phys.* **1952,** *20* (4), 722-725.

19. Brus, L., Electronic wave functions in semiconductor clusters: experiment and theory. *The Journal of Physical Chemistry* **1986,** *90* (12), 2555-2560.

20. Talapin, D. V.; Lee, J.-S.; Kovalenko, M. V.; Shevchenko, E. V., Prospects of Colloidal Nanocrystals for Electronic and Optoelectronic Applications. *Chem. Rev.* **2010,** *110* (1), 389-458.

21. Houtepen, A. J.; Hens, Z.; Owen, J. S.; Infante, I., On the Origin of Surface Traps in Colloidal II–VI Semiconductor Nanocrystals. *Chem. Mater.* **2017,** *29* (2), 752-761.

22. Boles, M. A.; Ling, D.; Hyeon, T.; Talapin, D. V., The surface science of nanocrystals. *Nat. Mater.* **2016,** *15*, 141.

23. Giansante, C.; Infante, I., Surface Traps in Colloidal Quantum Dots: A Combined Experimental and Theoretical Perspective. *J. Phys. Chem. Lett.* **2017,** *8* (20), 5209-5215.

24. Saba, M.; Aresti, M.; Quochi, F.; Marceddu, M.; Loi, M. A.; Huang, J.; Talapin, D. V.; Mura, A.; Bongiovanni, G., Light-Induced Charged and Trap States in Colloidal Nanocrystals

Detected by Variable Pulse Rate Photoluminescence Spectroscopy. *ACS Nano* **2013,** *7* (1), 229-238.

25. Rabouw, F. T.; Kamp, M.; van Dijk-Moes, R. J. A.; Gamelin, D. R.; Koenderink, A. F.; Meijerink, A.; Vanmaekelbergh, D., Delayed Exciton Emission and Its Relation to Blinking in CdSe Quantum Dots. *Nano Lett.* **2015,** *15* (11), 7718-7725.

26. Bawendi, M. G.; Wilson, W. L.; Rothberg, L.; Carroll, P. J.; Jedju, T. M.; Steigerwald, M. L.; Brus, L. E., Electronic structure and photoexcited-carrier dynamics in nanometer-size CdSe clusters. *Phys. Rev. Lett.* **1990,** *65* (13), 1623-1626.

27. Voznyy, O.; Thon, S. M.; Ip, A. H.; Sargent, E. H., Dynamic Trap Formation and Elimination in Colloidal Quantum Dots. *J. Phys. Chem. Lett.* **2013,** *4* (6), 987-992.

28. Boehme, S. C.; Azpiroz, J. M.; Aulin, Y. V.; Grozema, F. C.; Vanmaekelbergh, D.; Siebbeles, L. D. A.; Infante, I.; Houtepen, A. J., Density of Trap States and Auger-mediated Electron Trapping in CdTe Quantum-Dot Solids. *Nano Lett.* **2015,** *15* (5), 3056-3066.

29. Hwang, G. W.; Kim, D.; Cordero, J. M.; Wilson, M. W. B.; Chuang, C.-H. M.; Grossman, J. C.; Bawendi, M. G., Identifying and Eliminating Emissive Sub-bandgap States in Thin Films of PbS Nanocrystals. *Adv. Mater.* **2015,** *27* (30), 4481-4486.

30. Gómez-Campos, F. M.; Califano, M., Hole Surface Trapping in CdSe Nanocrystals: Dynamics, Rate Fluctuations, and Implications for Blinking. *Nano Lett.* **2012,** *12* (9), 4508-4517.

31. Hanifi, D. A.; Bronstein, N. D.; Koscher, B. A.; Nett, Z.; Swabeck, J. K.; Takano, K.; Schwartzberg, A. M.; Maserati, L.; Vandewal, K.; van de Burgt, Y.; Salleo, A.; Alivisatos, A. P., Redefining near-unity luminescence in quantum dots with photothermal threshold quantum yield. *Science* **2019,** *363* (6432), 1199.

32. Chen, O.; Zhao, J.; Chauhan, V. P.; Cui, J.; Wong, C.; Harris, D. K.; Wei, H.; Han, H.-S.; Fukumura, D.; Jain, R. K.; Bawendi, M. G., Compact high-quality CdSe–CdS core–shell nanocrystals with narrow emission linewidths and suppressed blinking. *Nat. Mater.* **2013,** *12*, 445.

33. Ding, T. X.; Olshansky, J. H.; Leone, S. R.; Alivisatos, A. P., Efficiency of Hole Transfer from Photoexcited Quantum Dots to Covalently Linked Molecular Species. *J. Am. Chem. Soc.* **2015,** *137* (5), 2021-2029.

34. Talapin, D.; Murray, C., PbSe Nanocrystal Solids for n- and p-Channel Thin Film Field-Effect Transistors. *Science* **2005,** *310*, 86-9.

35. Swarnkar, A.; Marshall, A. R.; Sanehira, E. M.; Chernomordik, B. D.; Moore, D. T.; Christians, J. A.; Chakrabarti, T.; Luther, J. M., Quantum dot–induced phase stabilization of α-$CsPbI_3$ perovskite for high-efficiency photovoltaics. *Science* **2016,** *354* (6308), 92-95.

36. Gao, Y.; Peng, X., Photogenerated Excitons in Plain Core CdSe Nanocrystals with Unity Radiative Decay in Single Channel: The Effects of Surface and Ligands. *J. Am. Chem. Soc.* **2015,** *137* (12), 4230-4235.

37. Pu, C.; Peng, X., To Battle Surface Traps on CdSe/CdS Core/Shell Nanocrystals: Shell Isolation versus Surface Treatment. *J. Am. Chem. Soc.* **2016,** *138* (26), 8134-8142.

38. Ip, A. H.; Thon, S. M.; Hoogland, S.; Voznyy, O.; Zhitomirsky, D.; Debnath, R.; Levina, L.; Rollny, L. R.; Carey, G. H.; Fischer, A.; Kemp, K. W.; Kramer, I. J.; Ning, Z.; Labelle, A. J.; Chou, K. W.; Amassian, A.; Sargent, E. H., Hybrid passivated colloidal quantum dot solids. *Nature Nanotechnology* **2012,** *7*, 577.

39. Kilina, S. V.; Tamukong, P. K.; Kilin, D. S., Surface Chemistry of Semiconducting Quantum Dots: Theoretical Perspectives. *Acc. Chem. Res.* **2016,** *49* (10), 2127-2135.

40. Green, M. L. H., A new approach to the formal classification of covalent compounds of the elements. *J. Organomet. Chem.* **1995,** *500* (1), 127-148.

41. Bruchez, M.; Moronne, M.; Gin, P.; Weiss, S.; Alivisatos, A. P., Semiconductor Nanocrystals as Fluorescent Biological Labels. *Science* **1998,** *281* (5385), 2013-2016.

42. Peterson, M. D.; Cass, L. C.; Harris, R. D.; Edme, K.; Sung, K.; Weiss, E. A., The Role of Ligands in Determining the Exciton Relaxation Dynamics in Semiconductor Quantum Dots. *Annu. Rev. Phys. Chem.* **2014,** *65* (1), 317-339.

43. Owen, J., The coordination chemistry of nanocrystal surfaces. *Science* **2015,** *347* (6222), 615-616.

44. Owen, J. S.; Park, J.; Trudeau, P.-E.; Alivisatos, A. P., Reaction Chemistry and Ligand Exchange at Cadmium−Selenide Nanocrystal Surfaces. *J. Am. Chem. Soc.* **2008,** *130* (37), 12279-12281.

45. Kovalenko, M. V.; Bodnarchuk, M. I.; Zaumseil, J.; Lee, J.-S.; Talapin, D. V., Expanding the Chemical Versatility of Colloidal Nanocrystals Capped with Molecular Metal Chalcogenide Ligands. *J. Am. Chem. Soc.* **2010,** *132* (29), 10085-10092.

46. Kagan, C. R.; Lifshitz, E.; Sargent, E. H.; Talapin, D. V., Building devices from colloidal quantum dots. *Science* **2016,** *353* (6302), aac5523.

47. Pringsheim, P., Zwei Bemerkungen über den Unterschied von Lumineszenz- und Temperaturstrahlung. *Zeitschrift für Physik* **1929,** *57* (11), 739-746.

48. Sheik-Bahae, M.; Epstein, R. I., Optical refrigeration. *Nature Photonics* **2007,** *1* (12), 693-699.

49. Batchelder, J. S.; Zewai, A. H.; Cole, T., Luminescent solar concentrators. 1: Theory of operation and techniques for performance evaluation. *Appl. Opt.* **1979,** *18* (18), 3090-3110.

50. Batchelder, J. S.; Zewail, A. H.; Cole, T., Luminescent solar concentrators. 2: Experimental and theoretical analysis of their possible efficiencies. *Appl. Opt.* **1981,** *20* (21), 3733-3754.

51. Bronstein, N. D.; Yao, Y.; Xu, L.; O'Brien, E.; Powers, A. S.; Ferry, V. E.; Alivisatos, A. P.; Nuzzo, R. G., Quantum Dot Luminescent Concentrator Cavity Exhibiting 30-fold Concentration. *ACS Photonics* **2015,** *2* (11), 1576-1583.

52. Protesescu, L.; Yakunin, S.; Bodnarchuk, M. I.; Krieg, F.; Caputo, R.; Hendon, C. H.; Yang, R. X.; Walsh, A.; Kovalenko, M. V., Nanocrystals of Cesium Lead Halide Perovskites ($CsPbX_3$, X = Cl, Br, and I): Novel Optoelectronic Materials Showing Bright Emission with Wide Color Gamut. *Nano Lett.* **2015,** *15* (6), 3692-3696.

53. Kovalenko, M. V.; Protesescu, L.; Bodnarchuk, M. I., Properties and potential optoelectronic applications of lead halide perovskite nanocrystals. *Science* **2017,** *358* (6364), 745-750.

54. Bosch, M. P.; Perez, R.; Lahuerta, G.; Hernanz, D.; Camps, F.; Guerrero, A., Difluoropalmitic Acids as Potential Inhibitors of the Biosynthesis of the Sex Pheromone of the Egyptian Armyworm Spodoptera littoralis - IV. *Biorg. Med. Chem.* **1996,** *4* (3), 6.

55. Yang, Z. Y.; Burton, D. J., Nickel-catalyzed reaction of iododifluoroacetates with alkenes and zinc: a novel and practical route to .alpha.,.alpha.-difluoro-functionalized esters and .alpha.,.alpha.,.omega.,.omega.-tetrafluoro diesters. *The Journal of Organic Chemistry* **1992,** *57* (19), 5144-5149.

56. Cottingham, P.; Brutchey, R. L., On the crystal structure of colloidally prepared CsPbBr3 quantum dots. *Chem. Commun.* **2016,** *52* (30), 5246-5249.

57. Ohmann, R.; Ono, L. K.; Kim, H.-S.; Lin, H.; Lee, M. V.; Li, Y.; Park, N.-G.; Qi, Y., Real-Space Imaging of the Atomic Structure of Organic–Inorganic Perovskite. *J. Am. Chem. Soc.* **2015,** *137* (51), 16049-16054.

58. De Roo, J.; Ibáñez, M.; Geiregat, P.; Nedelcu, G.; Walravens, W.; Maes, J.; Martins, J. C.; Van Driessche, I.; Kovalenko, M. V.; Hens, Z., Highly Dynamic Ligand Binding and Light Absorption Coefficient of Cesium Lead Bromide Perovskite Nanocrystals. *ACS Nano* **2016,** *10* (2), 2071-2081.

59. Anderson, N. C.; Hendricks, M. P.; Choi, J. J.; Owen, J. S., Ligand Exchange and the Stoichiometry of Metal Chalcogenide Nanocrystals: Spectroscopic Observation of Facile Metal-Carboxylate Displacement and Binding. *J. Am. Chem. Soc.* **2013,** *135* (49), 18536-18548.

60. Busby, E.; Anderson, N. C.; Owen, J. S.; Sfeir, M. Y., Effect of Surface Stoichiometry on Blinking and Hole Trapping Dynamics in CdSe Nanocrystals. *J. Phys. Chem. C* **2015,** *119* (49), 27797-27803.

61. ten Brinck, S.; Infante, I., Surface Termination, Morphology, and Bright Photoluminescence of Cesium Lead Halide Perovskite Nanocrystals. *ACS Energy Lett.* **2016,** *1* (6), 1266-1272.

62. Ravi, V. K.; Santra, P. K.; Joshi, N.; Chugh, J.; Singh, S. K.; Rensmo, H.; Ghosh, P.; Nag, A., Origin of the Substitution Mechanism for the Binding of Organic Ligands on the Surface of CsPbBr3 Perovskite Nanocubes. *J. Phys. Chem. Lett.* **2017,** *8* (20), 4988-4994.

63. Huang, X.; Paudel, T. R.; Dowben, P. A.; Dong, S.; Tsymbal, E. Y., Electronic structure and stability of the $CH_3NH_3PbBr_3$ (001) surface. *Phys. Rev. B* **2016,** *94* (19), 195309.

64. Buin, A.; Pietsch, P.; Xu, J.; Voznyy, O.; Ip, A. H.; Comin, R.; Sargent, E. H., Materials Processing Routes to Trap-Free Halide Perovskites. *Nano Lett.* **2014,** *14* (11), 6281-6286.

65. Uratani, H.; Yamashita, K., Charge Carrier Trapping at Surface Defects of Perovskite Solar Cell Absorbers: A First-Principles Study. *J. Phys. Chem. Lett.* **2017,** *8* (4), 742-746.

66. Kang, J.; Wang, L.-W., High Defect Tolerance in Lead Halide Perovskite CsPbBr3. *J. Phys. Chem. Lett.* **2017,** *8* (2), 489-493.

67. Philippe, B.; Park, B.-W.; Lindblad, R.; Oscarsson, J.; Ahmadi, S.; Johansson, E. M. J.; Rensmo, H., Chemical and Electronic Structure Characterization of Lead Halide Perovskites and Stability Behavior under Different Exposures—A Photoelectron Spectroscopy Investigation. *Chem. Mater.* **2015,** *27* (5), 1720-1731.

68. Dang, Z.; Shamsi, J.; Akkerman, Q. A.; Imran, M.; Bertoni, G.; Brescia, R.; Manna, L., Low-Temperature Electron Beam-Induced Transformations of Cesium Lead Halide Perovskite Nanocrystals. *ACS Omega* **2017,** *2* (9), 5660-5665.

69. Turo, M. J.; Macdonald, J. E., Crystal-Bound vs Surface-Bound Thiols on Nanocrystals. *ACS Nano* **2014,** *8* (10), 10205-10213.

70. Turo, M. J.; Shen, X.; Brandon, N. K.; Castillo, S.; Fall, A. M.; Pantelides, S. T.; Macdonald, J. E., Dual-mode crystal-bound and X-type passivation of quantum dots. *Chem. Commun.* **2016,** *52* (82), 12214-12217.

71. Koscher, B. A.; Swabeck, J. K.; Bronstein, N. D.; Alivisatos, A. P., Essentially Trap-Free CsPbBr3 Colloidal Nanocrystals by Postsynthetic Thiocyanate Surface Treatment. *J. Am. Chem. Soc.* **2017,** *139* (19), 6566-6569.

72. Ahmed, T.; Seth, S.; Samanta, A., Boosting the Photoluminescence of CsPbX3 (X = Cl, Br, I) Perovskite Nanocrystals Covering a Wide Wavelength Range by Postsynthetic Treatment with Tetrafluoroborate Salts. *Chem. Mater.* **2018,** *30* (11), 3633-3637.

73. Diroll, B. T.; Nedelcu, G.; Kovalenko, M. V.; Schaller, R. D., High-Temperature Photoluminescence of CsPbX3 (X = Cl, Br, I) Nanocrystals. *Adv. Funct. Mater.* **2017,** *27* (21), 1606750.

74. Sebastian, M.; Peters, J. A.; Stoumpos, C. C.; Im, J.; Kostina, S. S.; Liu, Z.; Kanatzidis, M. G.; Freeman, A. J.; Wessels, B. W., Excitonic emissions and above-band-gap luminescence in the single-crystal perovskite semiconductors $CsPbBr_3$ and $CsPbCl_3$. *Phys. Rev. B* **2015,** *92* (23), 235210.

75. Shi, H.; Du, M.-H., Shallow halogen vacancies in halide optoelectronic materials. *Phys. Rev. B* **2014,** *90* (17), 174103.

76. Mizusaki, J.; Arai, K.; Fueki, K., Ionic conduction of the perovskite-type halides. *Solid State Ionics* **1983,** *11* (3), 203-211.

77. Eames, C.; Frost, J. M.; Barnes, P. R. F.; O'Regan, B. C.; Walsh, A.; Islam, M. S., Ionic transport in hybrid lead iodide perovskite solar cells. *Nature Comm.* **2015,** *6*, 7497.

78. Akkerman, Q. A.; D'Innocenzo, V.; Accornero, S.; Scarpellini, A.; Petrozza, A.; Prato, M.; Manna, L., Tuning the Optical Properties of Cesium Lead Halide Perovskite Nanocrystals by Anion Exchange Reactions. *J. Am. Chem. Soc.* **2015,** *137* (32), 10276-10281.

79. Nedelcu, G.; Protesescu, L.; Yakunin, S.; Bodnarchuk, M. I.; Grotevent, M. J.; Kovalenko, M. V., Fast Anion-Exchange in Highly Luminescent Nanocrystals of Cesium Lead Halide Perovskites ($CsPbX_3$, X = Cl, Br, I). *Nano Lett.* **2015,** *15* (8), 5635-5640.

80. Moreels, I.; Fritzinger, B.; Martins, J. C.; Hens, Z., Surface Chemistry of Colloidal PbSe Nanocrystals. *J. Am. Chem. Soc.* **2008,** *130* (45), 15081-15086.

81. Kim, D.; Kim, D.-H.; Lee, J.-H.; Grossman, J. C., Impact of Stoichiometry on the Electronic Structure of PbS Quantum Dots. *Phys. Rev. Lett.* **2013,** *110* (19), 196802.

82. Rogach, A. L.; Franzl, T.; Klar, T. A.; Feldmann, J.; Gaponik, N.; Lesnyak, V.; Shavel, A.; Eychmüller, A.; Rakovich, Y. P.; Donegan, J. F., Aqueous Synthesis of Thiol-Capped CdTe Nanocrystals: State-of-the-Art. *J. Phys. Chem. C* **2007,** *111* (40), 14628-14637.

83. Jones, J. W.; Gibson, H. W., Ion Pairing and Host−Guest Complexation in Low Dielectric Constant Solvents. *J. Am. Chem. Soc.* **2003,** *125* (23), 7001-7004.

84. Udayabhaskararao, T.; Houben, L.; Cohen, H.; Menahem, M.; Pinkas, I.; Avram, L.; Wolf, T.; Teitelboim, A.; Leskes, M.; Yaffe, O.; Oron, D.; Kazes, M., A Mechanistic Study of Phase Transformation in Perovskite Nanocrystals Driven by Ligand Passivation. *Chem. Mater.* **2018,** *30* (1), 84-93.

85. Kleckner, I. R.; Foster, M. P., An introduction to NMR-based approaches for measuring protein dynamics. *Biochim. Biophys. Acta* **2011,** *1814* (8), 942-968.

86. Kresse, G.; Furthmüller, J., Efficient iterative schemes for ab initio total-energy calculations using a plane-wave basis set. *Phys. Rev. B* **1996,** *54* (16), 11169-11186.

87. Kresse, G.; Joubert, D., From ultrasoft pseudopotentials to the projector augmented-wave method. *Phys. Rev. B* **1999,** *59* (3), 1758-1775.

88. Heyd, J.; Scuseria, G. E.; Ernzerhof, M., Hybrid functionals based on a screened Coulomb potential. *J. Chem. Phys.* **2003,** *118* (18), 8207-8215.

89. Perdew, J. P.; Burke, K.; Ernzerhof, M., Generalized Gradient Approximation Made Simple. *Phys. Rev. Lett.* **1996,** *77* (18), 3865-3868.

90. Ravi, V. K.; Markad, G. B.; Nag, A., Band Edge Energies and Excitonic Transition Probabilities of Colloidal CsPbX3 (X = Cl, Br, I) Perovskite Nanocrystals. *ACS Energy Lett.* **2016,** *1* (4), 665-671.

91. Du, M.-H., Density Functional Calculations of Native Defects in $CH_3NH_3PbI_3$: Effects of Spin–Orbit Coupling and Self-Interaction Error. *J. Phys. Chem. Lett.* **2015,** *6* (8), 1461-1466.

92. Meggiolaro, D.; Motti, S. G.; Mosconi, E.; Barker, A. J.; Ball, J.; Andrea Riccardo Perini, C.; Deschler, F.; Petrozza, A.; De Angelis, F., Iodine chemistry determines the defect tolerance of lead-halide perovskites. *Energy & Environmental Science* **2018,** *11* (3), 702-713.

93. Azpiroz, J. M.; Ugalde, J. M.; Infante, I., Benchmark Assessment of Density Functional Methods on Group II–VI MX (M = Zn, Cd; X = S, Se, Te) Quantum Dots. *Journal of Chemical Theory and Computation* **2014,** *10* (1), 76-89.

94. Olshansky, J. H.; Ding, T. X.; Lee, Y. V.; Leone, S. R.; Alivisatos, A. P., Hole Transfer from Photoexcited Quantum Dots: The Relationship between Driving Force and Rate. *J. Am. Chem. Soc.* **2015,** *137* (49), 15567-15575.

95. Milstein, T. J.; Kroupa, D. M.; Gamelin, D. R., Picosecond Quantum Cutting Generates Photoluminescence Quantum Yields Over 100% in Ytterbium-Doped $CsPbCl_3$ Nanocrystals. *Nano Lett.* **2018,** *18* (6), 3792-3799.

96. Yettapu, G. R.; Talukdar, D.; Sarkar, S.; Swarnkar, A.; Nag, A.; Ghosh, P.; Mandal, P., Terahertz Conductivity within Colloidal $CsPbBr_3$ Perovskite Nanocrystals: Remarkably High Carrier Mobilities and Large Diffusion Lengths. *Nano Lett.* **2016,** *16* (8), 4838-4848.

97. Wu, K.; Liang, G.; Shang, Q.; Ren, Y.; Kong, D.; Lian, T., Ultrafast Interfacial Electron and Hole Transfer from $CsPbBr_3$ Perovskite Quantum Dots. *J. Am. Chem. Soc.* **2015,** *137* (40), 12792-12795.

98. Liu, F.; Zhang, Y.; Ding, C.; Kobayashi, S.; Izuishi, T.; Nakazawa, N.; Toyoda, T.; Ohta, T.; Hayase, S.; Minemoto, T.; Yoshino, K.; Dai, S.; Shen, Q., Highly Luminescent Phase-Stable CsPbI3 Perovskite Quantum Dots Achieving Near 100% Absolute Photoluminescence Quantum Yield. *ACS Nano* **2017,** *11* (10), 10373-10383.

99. He, J.; Vasenko, A. S.; Long, R.; Prezhdo, O. V., Halide Composition Controls Electron–Hole Recombination in Cesium–Lead Halide Perovskite Quantum Dots: A Time Domain Ab Initio Study. *J. Phys. Chem. Lett.* **2018,** *9* (8), 1872-1879.

100. Yin, Y.; Alivisatos, A. P., Colloidal nanocrystal synthesis and the organic–inorganic interface. *Nature* **2004,** *437*, 664.

101. Hens, Z.; Martins, J. C., A Solution NMR Toolbox for Characterizing the Surface Chemistry of Colloidal Nanocrystals. *Chem. Mater.* **2013,** *25* (8), 1211-1221.

102. Liu, Z.; Bekenstein, Y.; Ye, X.; Nguyen, S. C.; Swabeck, J.; Zhang, D.; Lee, S.-T.; Yang, P.; Ma, W.; Alivisatos, A. P., Ligand Mediated Transformation of Cesium Lead Bromide Perovskite Nanocrystals to Lead Depleted Cs_4PbBr_6 Nanocrystals. *J. Am. Chem. Soc.* **2017,** *139* (15), 5309-5312.

103. Palazon, F.; Almeida, G.; Akkerman, Q. A.; De Trizio, L.; Dang, Z.; Prato, M.; Manna, L., Changing the Dimensionality of Cesium Lead Bromide Nanocrystals by Reversible Postsynthesis Transformations with Amines. *Chem. Mater.* **2017,** *29* (10), 4167-4171.

104. Panina, N. S.; Belyaev, A. N.; Simanova, S. A., Carboxylic Acids and Their Anions. Acid and Ligand Properties. *Russ. J. Gen. Chem.* **2002,** *72* (1), 91-94.

105. Siggel, M. R. F.; Streitwieser, A.; Thomas, T. D., The role of resonance and inductive effects in the acidity of carboxylic acids. *J. Am. Chem. Soc.* **1988,** *110* (24), 8022-8028.

106. Fritzinger, B.; Moreels, I.; Lommens, P.; Koole, R.; Hens, Z.; Martins, J. C., In Situ Observation of Rapid Ligand Exchange in Colloidal Nanocrystal Suspensions Using Transfer NOE Nuclear Magnetic Resonance Spectroscopy. *J. Am. Chem. Soc.* **2009,** *131* (8), 3024-3032.

107. Clore, G. M.; Gronenborn, A. M., Theory and applications of the transferred nuclear overhauser effect to the study of the conformations of small ligands bound to proteins. *Journal of Magnetic Resonance* **1982,** *48* (3), 402-417.

108. Woo, J. Y.; Lee, S.; Lee, S.; Kim, W. D.; Lee, K.; Kim, K.; An, H. J.; Lee, D. C.; Jeong, S., Air-Stable PbSe Nanocrystals Passivated by Phosphonic Acids. *J. Am. Chem. Soc.* **2016,** *138* (3), 876-883.

109. Whitham, P. J.; Marchioro, A.; Knowles, K. E.; Kilburn, T. B.; Reid, P. J.; Gamelin, D. R., Single-Particle Photoluminescence Spectra, Blinking, and Delayed Luminescence of Colloidal CuInS2 Nanocrystals. *J. Phys. Chem. C* **2016,** *120* (30), 17136-17142.

110. Bae, W. K.; Padilha, L. A.; Park, Y.-S.; McDaniel, H.; Robel, I.; Pietryga, J. M.; Klimov, V. I., Controlled Alloying of the Core–Shell Interface in CdSe/CdS Quantum Dots for Suppression of Auger Recombination. *ACS Nano* **2013,** *7* (4), 3411-3419.

111. Fischer, S.; Bronstein, N. D.; Swabeck, J. K.; Chan, E. M.; Alivisatos, A. P., Precise Tuning of Surface Quenching for Luminescence Enhancement in Core–Shell Lanthanide-Doped Nanocrystals. *Nano Lett.* **2016,** *16* (11), 7241-7247.

112. Pan, J.; Quan, L. N.; Zhao, Y.; Peng, W.; Murali, B.; Sarmah, S. P.; Yuan, M.; Sinatra, L.; Alyami, N. M.; Liu, J.; Yassitepe, E.; Yang, Z.; Voznyy, O.; Comin, R.; Hedhili, M. N.; Mohammed, O. F.; Lu, Z. H.; Kim, D. H.; Sargent, E. H.; Bakr, O. M., Highly Efficient Perovskite-Quantum-Dot Light-Emitting Diodes by Surface Engineering. *Adv. Mater.* **2016,** *28* (39), 8718-8725.

113. Han, G.; Koh, T. M.; Lim, S. S.; Goh, T. W.; Guo, X.; Leow, S. W.; Begum, R.; Sum, T. C.; Mathews, N.; Mhaisalkar, S., Facile Method to Reduce Surface Defects and Trap Densities in Perovskite Photovoltaics. *ACS Appl. Mater. Interfaces* **2017,** *9* (25), 21292-21297.

114. Noel, N. K.; Abate, A.; Stranks, S. D.; Parrott, E. S.; Burlakov, V. M.; Goriely, A.; Snaith, H. J., Enhanced Photoluminescence and Solar Cell Performance via Lewis Base Passivation of Organic–Inorganic Lead Halide Perovskites. *ACS Nano* **2014,** *8* (10), 9815-9821.

115. Tan, Y.; Zou, Y.; Wu, L.; Huang, Q.; Yang, D.; Chen, M.; Ban, M.; Wu, C.; Wu, T.; Bai, S.; Song, T.; Zhang, Q.; Sun, B., Highly Luminescent and Stable Perovskite Nanocrystals with Octylphosphonic Acid as Ligand for Efficient Light Emitting Diodes. *ACS Appl. Mater. Interfaces* **2018,** *10* (4), 3784-3792.

116. Pan, J.; Sarmah, S. P.; Murali, B.; Dursun, I.; Peng, W.; Parida, M. R.; Liu, J.; Sinatra, L.; Alyami, N.; Zhao, C.; Alarousu, E.; Ng, T. K.; Ooi, B. S.; Bakr, O. M.; Mohammed, O. F., Air-Stable Surface-Passivated Perovskite Quantum Dots for Ultra-Robust, Single- and Two-Photon-Induced Amplified Spontaneous Emission. *J. Phys. Chem. Lett.* **2015,** *6* (24), 5027-5033.

117. Imran, M.; Caligiuri, V.; Wang, M.; Goldoni, L.; Prato, M.; Krahne, R.; De Trizio, L.; Manna, L., Benzoyl Halides as Alternative Precursors for the Colloidal Synthesis of Lead-Based Halide Perovskite Nanocrystals. *J. Am. Chem. Soc.* **2018,** *140* (7), 2656-2664.

118. Wu, Y.; Wei, C.; Li, X.; Li, Y.; Qiu, S.; Shen, W.; Cai, B.; Sun, Z.; Yang, D.; Deng, Z.; Zeng, H., In Situ Passivation of $PbBr_6^{4-}$ Octahedra toward Blue Luminescent CsPbBr3 Nanoplatelets with Near 100% Absolute Quantum Yield. *ACS Energy Lett.* **2018,** *3* (9), 2030-2037.